Pore-network modelling of non-Darcy flow through heterogeneous porous media

A. A. El-Zehairy[a,b,*], M. Mousavi Nezhad[a], V. Joekar-Niasar[c], I. Guymer[d], N. Kourra[e], M. A. Williams[e]

[a] School of Engineering, Univ. of Warwick, Coventry CV4 7AL, U.K.

[b] Irrigation & Hydraulic Engineering Dept., Faculty of Engineering, Mansoura Univ., Mansoura 35516, Egypt, el_zehairy@mans.edu.eg

[c] School of Chemical Engineering and Analytical Science, University of Manchester, M13 9PL Manchester, UK

[d] Department of Civil and Structural Engineering, University of Sheffield, Sheffield, UK

[e] IMC, WMG, Univ. of Warwick, Coventry CV4 7AL, U.K.

*Corresponding author: E-mail: A.el-zehairy@warwick.ac.uk

Abstract

A pore-network model (PNM) was developed to simulate non-Darcy flow through porous media. This paper investigates the impact of micro-scale heterogeneity of porous media on the inertial flow using pore-network modelling based on micro X-ray Computed Tomography (XCT) data. Laboratory experiments were carried out on a packed glass spheres sample at flow rates from 0.001 to 0.1 l/s. A pore-network was extracted from the 3D XCT scanned volume of the 50 mm diameter sample to verify the reliability of the model. The validated model was used to evaluate the role of micro-heterogeneity in natural rocks samples. The model was also used to investigate the effect of pore heterogeneity on the onset of the non-Darcy flow regime, and to estimate values of the Darcy permeability, Forchheimer coefficient and apparent permeability of the porous media. The numerical results show that the Reynold's number at which nonlinear flow occurs, is up to several orders of magnitude smaller for the heterogeneous porous domain in comparison with that for the homogeneous porous media. For the Estaillades carbonate rock sample, which has a high degree of heterogeneity, the resulting pressure distribution showed that the sample is composed of different zones, poorly connected to each other. The pressure values within each zone are nearly equal and this creates a number of stagnant zones within the sample and reduces the effective area for fluid flow. Consequently, the velocity distribution within the sample ranges from low, in stagnant zones, to high, at the connection between zones, where the inertial effects can be observed at a low pressure gradient.

Keywords: Non-Darcy Flow; Pore-network modelling; Forchheimer equation; heterogeneous porous media.

1. Introduction

Many engineering transport phenomena are controlled by flow through porous media. To reliably predict the flow, it is important to understand pore-scale factors and determine the boundaries between different flow regimes. Neglecting the non-linear inertial effects according to Stokes law, flow through porous media is usually modelled using Darcy's law (Equation 1) (Darcy, 1856).

$$-\frac{\Delta P}{L} = \frac{\mu}{K_D} v \tag{1}$$

Darcy's law is a linear relationship between the pressure drop (ΔP) between two points separated by distance (L) and the superficial or Darcy velocity ($v = \frac{q}{A}$), where q is the volumetric fluid discharge, A is the whole cross-sectional area perpendicular to the flow direction, μ is the fluid dynamic viscosity and K_D is the Darcy permeability. However, for higher velocities, i.e. when the pressure drop due to inertial effects is ≥ 1% of the total pressure loss (Section 2.2.2), Equation 1 is no longer valid, and the inertial terms cannot be neglected. Hence, the relationship between the pressure gradient and the superficial velocity becomes non-linear.

In porous media, inertial effects can be expressed in the form of drag forces, and as was shown by experiments, the pressure drop in such case is proportional to the summation of two terms; one term includes the fluid velocity and represents the force exerted to overcome fluid viscosity, whilst the other term includes the squared value of fluid velocity and represents the force exerted to overcome fluid-medium interactions. The second term represents the inertial effects which is a function of pore geometry, permeability and Reynold's number (Vafai & Tien, 1981; Zeng & Grigg, 2006). Flow through the hyporheic zone, near groundwater wells, or within hydraulic fractures in underground reservoirs are examples of flow in real environment that show non-Darcy behaviour. For the non-Darcy flow regime, normally the Forchheimer's equation is applied (Forchheimer, 1901). Forchheimer's equation (Equation 2) is an extension to Darcy's law and was developed by adding a quadratic velocity term to account for the non-linear inertial effects:

$$-\frac{\Delta P}{L} = \frac{\mu}{K_F} v + \rho \beta v^2 \quad (2)$$

where K_F is the Forchheimer permeability, that is very close to, but not the same as, Darcy permeability (K_D), and ρ is the fluid density. β is the non-Darcy coefficient, also known as Forchheimer coefficient, which is a medium dependent value similar to permeability. The non-Darcy coefficient accounts for the inertial effects due to convergence, divergence and tortuosity in the flow path geometry (Thauvin & Mohanty, 1998; Balhoff & Wheeler, 2009). Normally, the β coefficient and the onset of non-Darcy flow regime are determined experimentally, whereas some authors developed empirical relationships that predict β as a function of the medium permeability, porosity and tortuosity (e.g. Thauvin and Mohanty (1998) and Liu et al. (1995)).

To determine β and K_F from Forchheimer's equation, a linearized form of Equation 2 can be used to determine the relation between $\frac{\Delta P}{L\mu v}$ or $\frac{1}{K_{app}}$, where K_{app} is the apparent permeability, against $\frac{\rho v}{\mu}$. This should result in a straight line with slope β and intercept $1/K_F$ (Equation 3).

$$\frac{\Delta P}{L\mu v} = \frac{1}{K_{app}} = \frac{1}{K_F} + \beta \frac{\rho v}{\mu} \quad (3)$$

All experimental work has limitations, either due to difficulties or uncertainties in measuring some quantities, mainly rooted from the complexity of the process. In such cases, computational methods provide an alternative tool to gain insight into the processes. The computational methods used for studying flow in porous media can be divided into conventional continuum-scale numerical models and pore-scale models. Pore-scale models have advantages over the continuum-scale numerical models as they provide details of the physical process occurring at pore-scale, and their consequence at macroscale (Joekar-Niasar & Hassanizadeh, 2012). Moreover, the medium parameters estimated from pore-scale studies can be used to parameterize macro-scale equations (e.g. El-Zehairy et al., 2018).

To simulate single phase, incompressible, non-Darcy flow in a fully-saturated porous medium at the macro-scale, typically the Navier-Stokes equations are used, simplified, averaged over the simulation domains (fluid and solid phases), and then solved numerically. For example, Zimmerman et al. (2004) and Zhang and Xing (2012) solved Navier-Stokes equations for nonlinear flow using a finite-element mesh; Aly and Asai (2015) simulated non-Darcy flow through porous media by the incompressible smooth particle hydrodynamics method and Belhaj et al. (2003) used

the Forchheimer equation to derive a finite difference model for Darcy and non-Darcy flow in porous media. Many Computational Fluid Dynamics (CFD) software packages such as ANSYS CFX, Fluent, and OpenFOAM solve these equations. However, there are other models that can be used to simulate non-Darcy flow such as the Barree and Conway model, the hydraulic radius model, A. V. Shenoy's Model, and the Fractal Model. Further details about these models can be found in the review by Wu et al. (2016).

1.1. Pore-scale modelling:

Pore-scale models can be subdivided into six different groups: Lattice-Boltzmann (LB) models (e.g., Kuwata and Suga, 2015), smoothed particle hydrodynamics (SPH) approach (e.g., Bandara et al. 2013), level-set models (e.g., Akhlaghi Amiri and Hamouda, 2013), percolation models (e.g., Wilkinson, 1984), pore-network models (e.g., Bijeljic et al., 2004; Joekar-Niasar et al. 2009) (Joekar-Niasar & Hassanizadeh, 2012) and direct numerical simulation (DNS) (e.g., Raeini et al., 2012; Bijeljic et al., 2013b; Aziz et al., 2018). Percolation models cannot reveal any transient processes information and all other methods are computationally more expensive compared to pore-network models (Celia et al., 1995; Wang et al., 1999; Bijeljic et al., 2004; Bijeljic & Blunt, 2007; Joekar-Niasar & Hassanizadeh, 2012; Blunt et al., 2013; Oostrom et al., 2016). The SPH approach is a particle-based method, which although it has the advantage of not being constrained by lattice points (e.g. similar to Lattice Boltzmann), it is computationally more expensive (Tartakovsky et al., 2015). Dealing with a wide range of contact angles in the level set method is challenging and significant efforts are spent on that. DNS has been used mainly to simulate creeping flow through porous media, however, it could also be used to simulate other flow regimes (e.g. Muljadi et al., 2015). Using DNS, the Navier-Stokes equations are solved numerically on a mesh based on the voxelised X-ray Computed Tomography (XCT) data of the medium. Using large mesh elements or large time steps will lead to some errors at the small scales which will be transferred to the large scale and corrupt the solution (Poinsot et al., 1995; Moin & Mahesh, 1998; Alfonsi, 2011; Mousavi Nezhad & Javadi, 2011; Mousavi Nezhad et al., 2011).

In pore network modelling (PNM), the large pores constrained between the grains are referred to as pore bodies (PB). The pore bodies are connected to each other by narrow paths which are referred to as pore throats (PTh). Generally, the pore bodies are represented using spheres and the pore throats are represented by cylinders or conical shapes. However, there are some studies that

considered other shapes for pore bodies and pore throats to enhance the accuracy of model predictions (e.g. Joekar-Niasar et al., 2010). Connectivity is defined by the coordination number which is the number of pore throats connected to a pore body. The PNM approach can provide a simplified structure of complex porous media and allow the investigation of pore-scale processes. It can also provide details of flow velocities and pressure fields for complex heterogeneous pore spaces. Such information is essential to understand the flow behaviour and for studying solute transport in heterogenous porous media.

Although many researchers have used pore-network modelling to investigate flow through porous media, few have studied the flow within the laminar non-Darcy regime. The first study was conducted by Thauvin and Mohanty (1998) and was limited to 3D regular lattice pore-networks. To simulate the converging-diverging flow behaviour, Thauvin and Mohanty (1998) used modified forms of two equations originally proposed by Bird et al. (1960) for modelling pressure loss due to sudden expansion (diverging) and contraction (converging). Wang et al. (1999) extended Thauvin and Mohanty's work for modelling non-Darcy flow through anisotropic pore-networks, which was also limited to regular structured pore-networks. Later, Lao et al. (2004) performed a study of non-Darcy flow using the Forchheimer equation implemented in a two-dimensional random irregular pore-network with the maximum coordination number of three. In another study, Lemley et al. (2007) used the Forchheimer equation to simulate flow in a random unstructured three-dimensional (3D) pore-network, with the upper limit of the coordination number in their network also three. The most recent study for non-Darcy flow through 3D irregular unstructured pore-networks using the Forchheimer equation is the work of Balhoff and Wheeler (2009). They argued that the equations presented by Bird et al. (1960), are valid only for turbulent flow, despite the fact that these equations can be derived from Bernoulli, continuity and momentum equations, so they are valid for all flow conditions including laminar flow. Balhoff and Wheeler (2009) approximated the geometry of pore throats by axisymmetric sinusoidal ducts and calculated the pressure loss through these throats by solving the Navier-Stokes equations using a finite element method (FEM). After doing the FEM simulations for pore throats with different dimensions, they provided a relatively complex approximated equation that describes the pressure loss due to expansion and contraction through each pore throat. Their equation depends on the flow rate and the pore throat and the pore body geometries. However, their equation was developed for axisymmetric ducts, and they defined the geometries of these ducts by a sinusoidal equation

that implies the pore bodies at the two ends of a pore throat to have an equal size, which is not likely to happen in real porous media. None of these mentioned previous studies investigated the effect of pore body and pore throat shape factors (G) on the flow simulation, which is considered of high importance for natural porous media containing pores with irregular shapes. It is also necessary for simulating two or multi-phase flow within the non-Darcy flow regime.

In porous media, heterogeneity can be expressed as the variation in shapes, sizes and interconnectivity of the pores. Sahimi (2011) divided the heterogeneity of natural media into four main categories; microscopic heterogeneities, macroscopic heterogeneities, field-scale heterogeneities and gigascopic heterogeneities. Large-scale reservoirs can only be fully determined if their measurable properties and features are detected at these different length scales. With the help of modern imaging techniques, the internal morphologies of highly complex material can be visualized and quantified in 3D. These geometric properties can be detected at the resolution of few microns, with a field of view of a few millimetres (Knackstedt et al., 2001).

In this paper, a 3D pore-network model was developed to simulate non-Darcy laminar flow through porous media to address the impact of pore heterogeneity on the inertial flow and hydraulic properties of the porous media. The model has been verified against experimental data from packed glass spheres and some numerical results achieved through direct numerical simulations. This work particularly focuses on the simulation of flow through natural porous media using micro XCT 3D images. The effect of pore-scale flow processes (e.g. expansion and contraction of flow) on macro-scale inertial flow behaviour has been investigated. It is important to determine the velocity threshold above which the Darcy's law is not valid and a non-Darcy model should be applied. Therefore, the model is applied to four porous media with different structures and degrees of heterogeneity. The onset of a non-Darcy flow regime for each sample has been determined, discussed and compared to previous research.

2. Methodology

2.1. Pore-network extraction

The reliability of predictions from pore-network modelling depends on firstly how accurately the approximated pore-network represents the porous medium; and secondly, on the accuracy of

equations and the numerical schemes used for simulating the physical or chemical process in the porous medium (Balhoff & Wheeler, 2009).

Pore-networks can be generated in three ways. The first approach is to extract the pore-network directly from 3D images obtained using imaging technologies, such as XCT imaging, focused ion beams, scanning electron microscopy and nuclear magnetic resonance (Xiong et al., 2016). The second approach generates a representative pore-network using (geo)statistical information such as pore body and pore throat size distributions, throat length distribution, coordination number distribution and spatial correlation length (Al-Raoush et al., 2003; Gao et al., 2012; Babaei & Joekar-Niasar, 2016). The third approach, the grain-based model, generates a pore-network based on the solid phase properties such as grain diameters and grain positions (Bryant & Blunt, 1992). This approach was further extended to generate pore-networks from grains affected by swelling, compaction or sedimentation (e.g. Bryant et al., 1993).

In this study, for verification purposes, the first method is used to extract the pore-networks from four XCT 3D images: one packed glass spheres with average diameter (d_{avg}) = 1.84 mm, which is the same sample used in the experimental work, and the three other samples of beadpack, Bentheimer sandstone, and Estaillades carbonate published in Muljadi et al. (2015) using the pore-network extraction code developed by Raeini et al. (2017). The pore-network extraction code can generate pore bodies and pore throats with triangular, square or circular cross-sections. The shape of the pore cross-sections is selected based on the level of irregularity over the wall of the narrow pores, which is quantified with shape factor, *G*. The shape factor is a dimensionless parameter, defined as $G = \frac{a}{p^2}$, where a is the average cross-sectional area of the pore throat or the pore body and p is the average perimeter (Mason & Morrow, 1991; Valvatne & Blunt, 2004). The value of the shape factor decreases when the shape of the surface of the pore space wall becomes irregular. According to geometrical definitions of 2D geometries, the value of shape factor ranges from zero, for a slit shape triangle, to $\frac{\sqrt{3}}{36}$ for equilateral triangle, whilst for squares and circles, the shape factor has values of $\frac{1}{16}$ and $\frac{1}{4\pi}$, respectively (Oren et al., 1998; Valvatne & Blunt, 2004). The shape factor definition for more complex geometries such as hyperbolic polygonal cross-sections can be found in Joekar-Niasar et al. (2010).

2.2. Mathematical modelling

2.2.1. Darcy flow modelling

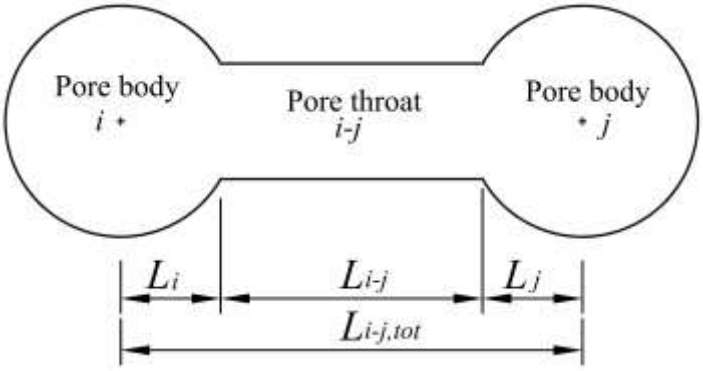

Fig. 1 Schematic of a pore throat (*i-j*) and two pore bodies (*i* and *j*).

In Darcy flow, the inertial effects are neglected and the flow rate (q_{i-j}) between two pore bodies *i* and *j* is given analytically by Hagen–Poiseuille equation (Hagen, 1839; Poiseuille, 1841)

$$q_{i-j} = K_{i-j,tot}\,\Delta P^{v}_{i-j} = \frac{g_{i-j,tot}}{L_{i-j,tot}}\Delta P^{v}_{i-j} \tag{4}$$

Where $K_{i-j,tot} = \frac{g_{i-j,tot}}{L_{i-j,tot}}$, $g_{i-j,tot}$ is the fluid conductance, $L_{i-j,tot}$ is the length between the two pore body centres and ΔP^{v}_{i-j} represents the viscous pressure drop between the two pore bodies *i* and *j*. The conductance between the two pore bodies *i* and *j* is defined as harmonic mean of the conductances through the pore throat and the connected pore bodies (Oren et al., 1998; Valvatne & Blunt, 2004), given by

$$\frac{L_{i-j,tot}}{g_{i-j,tot}} = \frac{L_i}{g_i} + \frac{L_{i-j}}{g_{i-j}} + \frac{L_j}{g_j} \tag{5}$$

where *i-j* indicates the connecting throat, $L_{i\text{-}j}$ is the pore throat length excluding the lengths of the two connected pore bodies *i* and *j*, L_i and L_j are the pore body lengths from the pore throat interface to the pore centre (Fig. 1). For laminar flow in a circular tube the conductance g_{pore} is given analytically by the Hagen–Poiseuille equation (Hagen, 1839; Poiseuille, 1841)

$$g_{pore} = k\frac{a^2 G}{\mu} = \frac{1}{2}\frac{a^2 G}{\mu} \tag{6}$$

For equilateral triangular and square cross-sections, analytical expression can also be developed (Patzek & Silin, 2001; Valvatne & Blunt, 2004) with *k* equal to 3/5 and 0.5623 respectively. It has been also found that the conductance of irregular triangles can be approximated by equation (6), using the same constant (k = 3/5) as for an equilateral triangle (Oren et al., 1998; Valvatne & Blunt, 2004). The pore cross-sectional area (a) can be related to the shape factor as $a = \frac{r^2}{4G}$, where r is the radius of the inscribed circle inside the pore (Oren et al., 1998).

For each pore body i, considering incompressible steady flow, the mass conservation can be expressed as

$$\sum_{j \in N_i} q_{i-j} = 0 \tag{7}$$

where N_i is the coordination number of pore body i.

For the whole pore-network, Equation 4 is applied for each pore throat and Equation 7 is invoked at each pore body. In all simulations, no-flow boundary condition is applied for all pore-network boundaries except the inlet and outlet boundaries where constant pressure values are applied. This process results in a system of N linear equations, where N is the total number of pore bodies in the pore-network. Solving this system of equations using the method described in Babaei and Joekar-Niasar (2016), the pressure value at each node can be obtained and by applying Equation (4), the discharge through each pore throat can be estimated. Finally, the overall permeability (K_D) of the pore-network can be obtained by applying Darcy's law (Equation 1) for the whole pore-network.

In all simulations, the same fluid parameters used by Muljadi et al. (2015) are applied, water is considered as the working fluid with dynamic viscosity μ = 0.001 kg/ms and density ρ = 1000 kg/m^3. The overall volumetric fluid discharge q is obtained by summing all pore throat discharges either at the inlet or the outlet of the pore-network, while the flow superficial velocity (v) is estimated as $v = \frac{q}{A}$. However, for highly heterogeneous media such as Estaillades carbonate, the pore's cross-sectional area may differ significantly from one location to another, so using the whole cross-sectional area will cause uncertainties in q and K_D values. For that reason, for Estaillades carbonate, the average pore velocity is estimated, then the superficial velocity (v) is derived as the average pore velocity times the medium porosity (ϕ).

2.2.2. Non-Darcy flow modelling

Following Muljadi et al. (2015) and Comiti et al. (2000), the onset of non-Darcy flow is assumed to be the point at which the pressure drop due to the linear term becomes less than 99% of the total pressure drop. Using $\sqrt{K_D}$ to replace the characteristic length (L_{charc}) in the conventional Reynold's number (Re_L), so

$$Re_L = \frac{\rho\, v\, L_{\text{charc}}}{\mu} \tag{8}$$

$$Re_K = \frac{\rho\, v \sqrt{K_D}}{\mu} \tag{9}$$

where $\sqrt{K_D}$ is the Brinkman screening length (Durlofsky & Brady, 1987), i.e. the characteristic length is replaced by the square root of Darcy permeability to give the permeability based Reynold's number (Re_K).

For relatively high flow velocities, the inertial effects cannot be neglected as in the Darcy creeping flow regime. To consider the inertial effects due to expansion, when flow moves from a pore throat to a connected pore body, and contraction, when flow moves from a pore body to a connected pore throat, the pressure loss due to these two processes should be considered in the calculation of total pressure drop through any pore throat. In the developed model, the pressure losses due to the inertial effects, expansion and contraction, are expressed using equations 10 and 11 (Kays, 1950; Abdelall et al., 2005; Guo et al., 2010; Momen et al., 2016).

$$\Delta P_{i-j}^{exp} = K_e \frac{\rho v_{i-j}^2}{2} = \left[\left(\frac{a_{i-j}}{a_j}\right)^2 \left(2\, kd_j - \alpha_j\right) + \alpha_{i-j} - 2\, kd_{i-j}\left(\frac{a_{i-j}}{a_j}\right)\right] \frac{\rho v_{i-j}^2}{2} \tag{10}$$

where ΔP_{i-j}^{exp} is the pressure loss due to expansion, K_e is the expansion coefficient, a_{i-j} and a_j are the cross-sectional areas of the pore throat and the connected pore body *j*, and v_{i-j} is the average fluid velocity through pore throat that connects the two pore bodies *i* and *j*. *kd* and α are the dimensionless momentum and kinetic-energy coefficients which depend on the velocity profile in each pore. For laminar flow, when the velocity is low and its profile is parabolic, *kd* is equal to 1.33, 1.39 and 1.43 for circular, square and equilateral triangular cross-sections respectively, while α is equal to 2 for circular cross-sections. For turbulent flow, when the velocity is high and its profile is almost uniform, *kd* and α are equal to ~1.0 (Kays, 1950).

$$\Delta P_{i-j}^{cont} = K_c \frac{\rho v_{i-j}^2}{2} = \left\{ \frac{1-\left[\alpha_{i-j}\left(\frac{a_{i-j}}{a_j}\right)^2 - 2\,kd_{i-j} + 1 - \left(\frac{a_{i-j}}{a_j}\right)^2\right] Cc^2 - 2Cc}{Cc^2} \right\} \frac{\rho v_{i-j}^2}{2} \quad (11)$$

$$Cc = 1 - \frac{1 - \frac{a_{i-j}}{a_j}}{2.08\left(1 - \frac{a_{i-j}}{a_j}\right) + 0.5371} \quad (12)$$

where ΔP_{i-j}^{cont} is the pressure loss due to contraction, K_c is the contraction coefficient, a_i is the cross-sectional area of the connected pore body *i*, *Cc* is the dimensionless jet contraction-area ratio (Vena-contraction) which can be estimated using Equation 12 (Geiger, 1964).

It has been found that using *kd* and α equal to 1.0 provides better representation of the non-Darcy flow which is characterised by higher velocities compared to the Darcy flow. This also agrees with the experimental findings of Abdelall et al. (2005) and Guo et al. (2010) performed on small channels. They showed that when using *kd* = 1.33 or α = 2.0 in equations 10 and 11, this result in overestimation of K_e and K_c in most of the cases they tested. Moreover, when flow passes through a sudden expansion or contraction, this creates eddies and turbulence that make a flat velocity profile a better approximation for the flow. Using *kd* and α equal to 1.0, equations 10 and 11 can be simplified and this results in the well-known Borda-Carnot equations (Crane, 1942; Bird et al., 1961).

The total pressure loss for any pore throat in the network can be given according to Equation 13 as follows:

$$\Delta P_{i-j}^{tot} = \Delta P_{i-j}^{v} + \Delta P_{i-j}^{exp} + \Delta P_{i-j}^{cont} = \left[\frac{L_{i-j,tot}}{g_{i-j,tot}}\right] q_{i-j} + K_e \frac{\rho q_{i-j}^2}{2a_{i-j}^2} + K_c \frac{\rho q_{i-j}^2}{2a_{i-j}^2}, \quad (13)$$

which can be written as

$$A_o\, q_{i-j}^2 + B_o\, q_{i-j} + C_o = 0.0 \quad (14)$$

where

$$A_o = [K_e + K_c]\frac{\rho}{2a_{i-j}^2},\ B_o = \left[\frac{L_{i-j,tot}}{g_{i-j,tot}}\right],\ C_o = -\Delta P_{i-j}^{tot}$$

To apply the continuity equation at each node, Equation 13 is rewritten in the form of a simple quadratic equation (Equation 14), its positive root is equal to $q_{i-j} = \frac{-B_o + \sqrt{{B_o}^2 - 4A_oC_o}}{2A_o}$. For the whole

pore-network, Equation 13 is applied for each pore throat and Equation 7 is invoked at each pore body. This process results in a system of N non-linear equations, where N is the total number of pore bodies in the pore-network. A FORTRAN code was developed with the use of HSL NS23 routine (HSL, 2013) to solve the resulting system of equations. The initial guess of the pressure values at each node is provided from the Darcy flow case, then the HSL NS23 routine iterates until the final solution is achieved within an acceptable predefined error criterion (until the sum of squares of residuals is less than 10^{-10}). By solving this nonlinear system of equations, the pressure value at each node can be obtained and the discharge through each pore throat is estimated by applying Equation 13. Finally, the non-Darcy coefficient (β) and Forchheimer permeability (K_F) can be obtained by fitting a linear relationship to the obtained results when $\frac{1}{K_{app}}$ is plotted against $\frac{\rho v}{\mu}$ (see Equation 3).

2.3. XCT-scanning and experimental work

To validate the proposed model, a porous medium sample (referred to as "packed spheres") composed of uniform spherical glass beads, with an average diameter (d_{avg}) of 1.84 ± 0.14 mm was packed in a Perspex circular pipe of 300 mm length and 50 mm internal diameter. The porous sample was placed in a recirculating pipe system with a sump of approximately 2.5 m^3. Water was used as a working fluid at different discharges ranging from 0.001 to 0.1 l/s. For each run, the discharge was measured manually. The head loss measurements were performed using two manometer tubes located 50 mm distance after the sample inlet and before the sample outlet to eliminate the effect of boundaries on the flow, i.e. the head loss was measured through a distance of 200 mm in the porous medium. To ensure the accuracy of manometric measurements at low pressure gradients, an SPI digital depth gauge with accuracy $\pm$ 0.01 mm was used to measure the manometric heads inside fixed, 25 mm wide manometric tubes. Moreover, before taking any measurements, water was allowed to run through the recirculating system for a period sufficient to remove any air from the system.

The middle part of the packed spheres sample used in the experimental work, which has the dimensions of 50 mm × 50 mm × 177 mm, was scanned to determine the representative elementary volume (REV) and to extract the equivalent pore-network. An REV can be defined as a representative portion or subvolume of the medium, when selecting such volume at different

location in the sample, the resulting parameters (ϕ, K_D or β) of the subvolumes should not vary significantly (Bear, 1972). To find an REV of the sample, a conventional approach was followed, a code was written to generate random coordinates of cubic subvolumes with different cube lengths (5, 10, 15, 20, 25, 30, 35 and 50 mm), and 10 different crops at random locations have been tested for each cube size. For each single crop, a pore-network was extracted, and the proposed pore-network model was used to estimate the porosity (ϕ), Darcy-permeability (K_D) and non-Darcy coefficient (β), as in Section 3.3.

Four XCT scans were performed to examine the packed spheres sample utilising Nikon XT H 225/320 LC. The XCT settings were chosen to achieve optimum penetration and minimise noise based on the grey values of the radiographs. A physical radiation filter of Tin (Sn) was used to reduce beam hardening and cupping errors. The resolution of the scans was achieved based on the diameter of the specimen. The scans were combined to provide the full volume of the medium.

3. Results and discussion

3.1. Determining the representative elementary volume (REV)

Fig. 2 shows the effect of cube lengths on determining the porous medium properties. It can be produced by applying the proposed model to the pore-networks extracted from all subvolume crops of the packed spheres CT-image. In Fig. 2, it is observed that a suitable REV might be a cube with length of 30 mm, which is a common value of the plateaus in figures 2a, 2b and 2c associated with minimum fluctuation, i.e. minimum standard deviation. However, this is not the case for the relatively small sample of 50 mm diameter used in the laboratory, considering its large average bead diameter of 1.84 mm. For this specific case, using REV length less than 50 mm will result in eliminating the effect of the containing pipe wall or boundaries. Due to the small size of the sample, the boundaries of the containing pipe have an effect on the estimated medium parameter as shown in Fig. 2. For that reason, an REV cube length of 50 mm was selected to consider the effect of external pipe on the medium structure and on the flow behaviour through the medium.

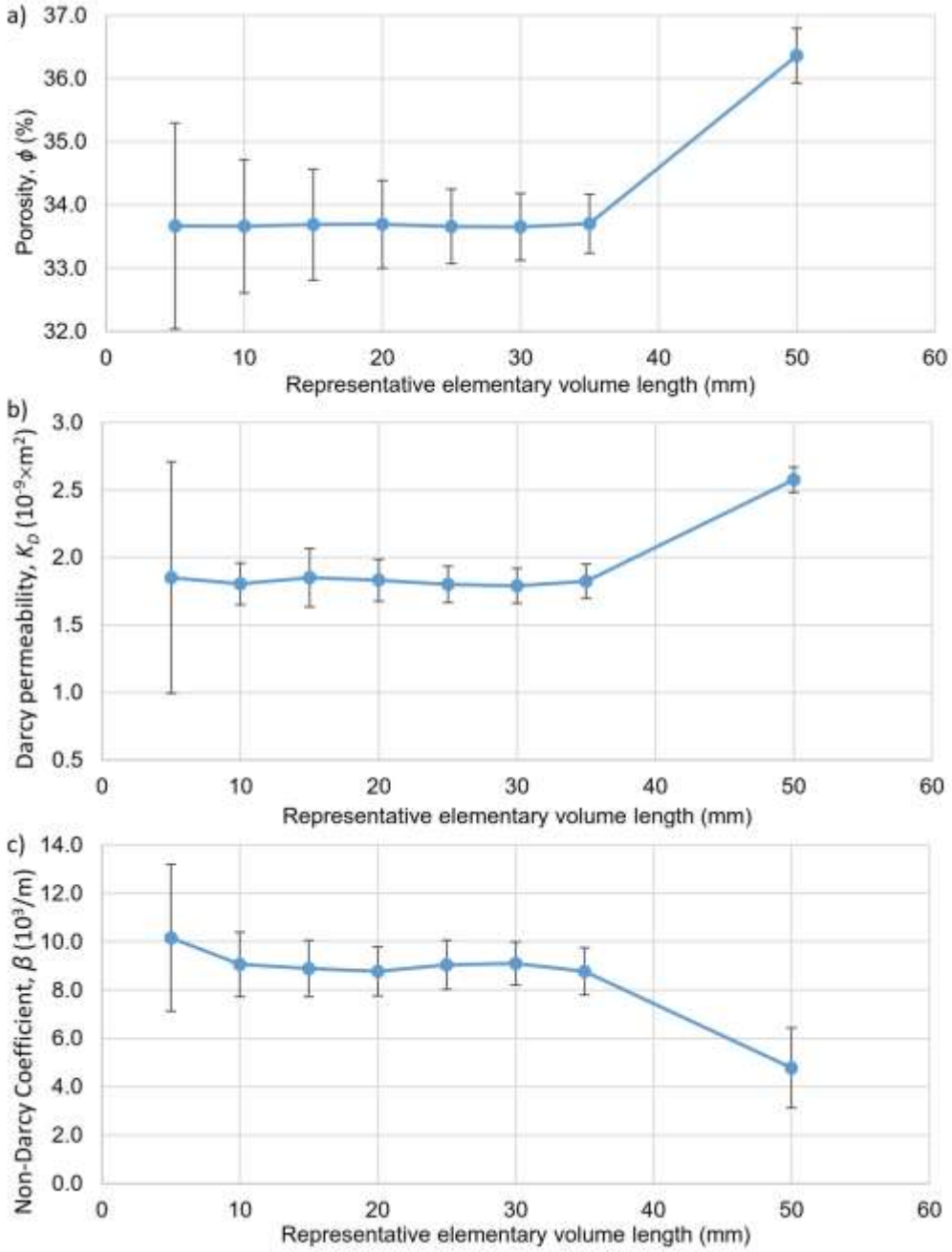

Fig. 2 Variation of a) porosity, b) Darcy-permeability and c) non-Darcy coefficient for different cubic subvolumes (10 crops for each REV length). The error bars represent the standard deviation of the estimated parameter for each REV length.

3.2. Extracted pore-networks from CT-images

Properties of the CT-images used to extract each of the four pore-networks shown in Fig. 3 are provided in Table 1.

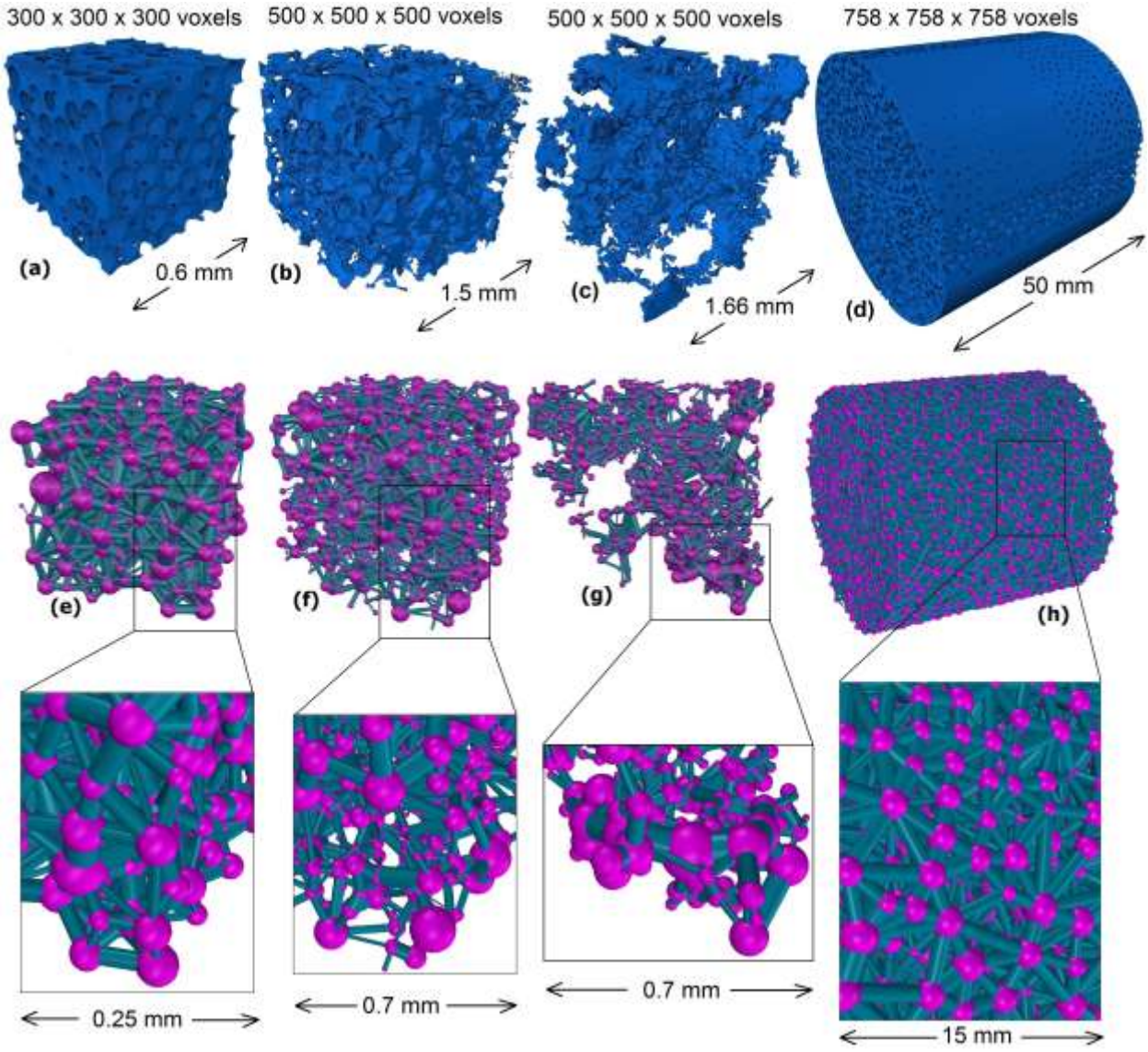

Fig. 3 The pore spaces of (a) beadpack, (b) Bentheimer, (c) Estaillades and (d) packed spheres (d_{avg} = 1.84 mm), and the equivalent pore-networks (e), (f), (g) and (h) respectively.

Table 1*: The properties and characteristics length of the samples.

Sample	Resolution (μm)	Porosity, ϕ	Characteristic length, L_{charc} (μm)	Total voxels	Pore voxels	$K_D \times 10^{-12}$ (m^2) obtained by Muljadi et al. (2015) or in the experiments.
Beadpack	2.0	0.359	100	300×300×300	9,700,082	5.57
Bentheimer	3.0035	0.211	139.9	500×500×500	26,413,875	3.50
Estaillades	3.3113	0.108	253.2	500×500×500	13,522,500	0.17

Packed spheres (d_{avg} =1.84 mm)	65.99	0.364	1,837	758×758×758	124,612,700	2250

*For the first three samples, the characteristic length (L_{charc}) values are obtained from Muljadi et al. (2015); for the unconsolidated beadpack they chose L_{charc} = 100 µm, while for consolidate porous media (Bentheimer and Estaillades) they followed the methodology in Mostaghimi et al. (2012) to determine L_{charc} as a function of the specific surface area of the pore-grain interface (the surface area divided by the whole volume including pores and grains). For the packed spheres (d_{avg} = 1.84 mm) sample, the characteristic length (L_{charc}) is the beads average diameter (d_{avg}).

The 300×300×300 voxels beadpack image (Fig. 3a) represents a random packing of spheres of uniform size. The image was created by Prodanović and Bryant (2006) to represent the experimental measurements of the sphere centres obtained by Finney (1970). The only available CT-image of Bentheimer sandstone sample used by Muljadi et al. (2015) is a 1000×1000×1000 voxels image. Unfortunately, the 500×500×500 voxels cropped image used in their work is not available. Few trials were performed to crop that large image into a 500×500×500 voxels image at arbitrary locations, but this resulted in properties different to those reported by Muljadi et al. (2015). To cope with that, the first 500 voxels in X, Y, and Z directions of the large image (1000×1000×1000 voxels) were arbitrary cropped, then the pore-network was extracted from that cropped image. This process will result in some uncertainties with respect to the Bentheimer sandstone sample. The extracted pore-network properties of the beadpack, Bentheimer sandstone, Estaillades carbonate and REV of the packed spheres (d_{avg} = 1.84 mm) samples are shown in Table 2 and Fig. 3e-h. The histograms of inscribed pore body and pore throat radii distributions for the four samples are shown in Fig.4.

Investigations on pore-scale flow behaviour and the morphological characteristics of Bentheimer sandstone and Estaillades carbonate, have revealed that Estaillades is more heterogeneous than Bentheimer (Bijeljic et al., 2013a; Bijeljic et al., 2013b; Guadagnini et al., 2014; Muljadi et al., 2015). This was also confirmed by plotting the semi-variograms of pore body radii and coordination numbers of each sample (Figure S1 and S2 in supplementary materials).

Table 2: The properties of the extracted pore-networks.

Sample	Beadpack	Bentheimer (500×500×500 voxels)	Estaillades	Packed spheres (d_{avg} = 1.84 mm)

Number of PBs	347	1033	954	10315
Number of PThs	1424	2418	1649	53960
Average coordination number	7.9	4.5	3.4	10.4
Maximum coordination number	21	23	19	30
Maximum inscribed PB radius (mm)	0.0344	0.0862	0.0692	0.7673
Average inscribed PB radius (mm)	0.0178	0.0231	0.0196	0.4103
Minimum inscribed PB radius (mm)	0.0051	0.0058	0.0064	0.1408
Maximum inscribed PTh radius (mm)	0.0287	0.0571	0.0575	0.6958
Average inscribed PTh radius (mm)	0.0089	0.0122	0.0116	0.1952
Minimum inscribed PTh radius (mm)	0.0009	0.0015	0.0016	0.0320

374

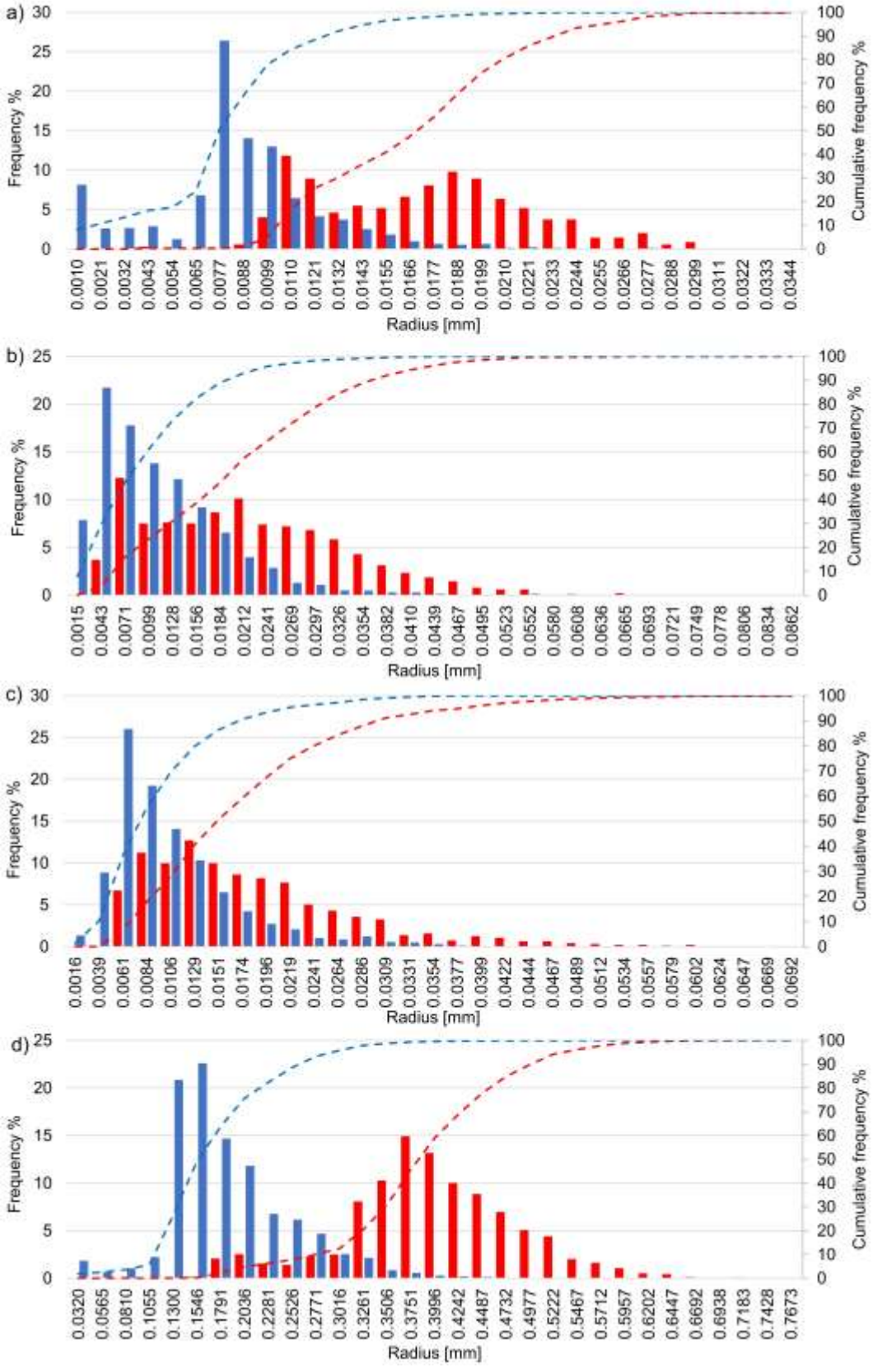
a)
Frequency %
Cumulative frequency %
Radius [mm]
0.0010 0.0021 0.0032 0.0043 0.0054 0.0065 0.0077 0.0088 0.0099 0.0110 0.0121 0.0132 0.0143 0.0155 0.0166 0.0177 0.0188 0.0199 0.0210 0.0221 0.0233 0.0244 0.0255 0.0266 0.0277 0.0288 0.0299 0.0311 0.0322 0.0333 0.0344
b)
Frequency %
Cumulative frequency %
Radius [mm]
0.0015 0.0043 0.0071 0.0099 0.0128 0.0156 0.0184 0.0212 0.0241 0.0269 0.0297 0.0326 0.0354 0.0382 0.0410 0.0439 0.0467 0.0495 0.0523 0.0552 0.0580 0.0608 0.0636 0.0665 0.0693 0.0721 0.0749 0.0778 0.0806 0.0834 0.0862
c)
Frequency %
Cumulative frequency %
Radius [mm]
0.0016 0.0039 0.0061 0.0084 0.0106 0.0129 0.0151 0.0174 0.0196 0.0219 0.0241 0.0264 0.0286 0.0309 0.0331 0.0354 0.0377 0.0399 0.0422 0.0444 0.0467 0.0489 0.0512 0.0534 0.0557 0.0579 0.0602 0.0624 0.0647 0.0669 0.0692
d)
Frequency %
Cumulative frequency %
Radius [mm]
0.0320 0.0565 0.0810 0.1055 0.1300 0.1546 0.1791 0.2036 0.2281 0.2526 0.2771 0.3016 0.3261 0.3506 0.3751 0.3996 0.4242 0.4487 0.4732 0.4977 0.5222 0.5467 0.5712 0.5957 0.6202 0.6447 0.6692 0.6938 0.7183 0.7428 0.7673

375

Fig. 4 Histograms of inscribed pore body and pore throat radii for the four samples; a) beadpack, b) Bentheimer, c) Estaillades and d) packed spheres.

3.3. Darcy permeability (K_D) and the non-Darcy coefficient (β)

The Darcy permeability (K_D) values obtained from PNM, by applying Darcy's law while neglecting the inertial effects, are in a good match (varying less than 15.2%) with the corresponding values in Muljadi et al. (2015) or obtained from experiments, as presented in Table 3. Relatively large discrepancies (14% and 15.2%) are observed for Bentheimer and the packed spheres (d_{avg}=1.84 mm) because the large Bentheimer image was cropped in an arbitrary location and because the packed spheres sample was scanned prior to experiments, so during experiments the position of some particles might have changed slightly under the effect of flow at large velocities. Also, the pore-network extraction code defines the parameters of pore-network elements using single phase direct numerical simulation on the CT-image, these details can be found in Raeini et al. (2017) and Raeini et al. (2018). That is why the PNM simulations can accurately reproduce the results predicted with direct simulation (by Muljadi et al., 2015) and differ from the results achieved by experiments.

Fig. 5 shows a Forchheimer plot which is a plot of the inverse of apparent permeability $\left(\frac{1}{K_{app}}\right)$ versus $\left(\frac{\rho v}{\mu}\right)$. The slope of each graph represents the non-Darcy coefficient (β) and it is equal to 1.49×10^5, 4.67×10^6, 2.82×10^8 and 5.232×10^3 (1/m) for Beadpack, Bentheimer, Estaillades and packed spheres, respectively. The corresponding β values obtained from Muljadi et al. (2015) and in the Laboratory are 2.57×10^5, 2.07×10^6, 6.15×10^8 and 10.87×10^3 (1/m), see Table 3. It is noticeable that β values from PNM are in good match (within the same order of magnitude and with maximum variation of 54%) with the values obtained by Muljadi et al. (2015) except Bentheimer which has larger discrepancy (126%) because the cropped image used differs from the image used by Muljadi et al. (2015). These discrepancies related to β values might be because of the simplifications of pore shapes during the pore-network extraction. The shift in the horizontal part of each curve when comparing PNM results to these by Muljadi et al. (2015), or from experiments, are due to the difference in K_D obtained from different methodologies, whilst the trend of each curve depends mainly on the pressure losses obtained at different velocities.

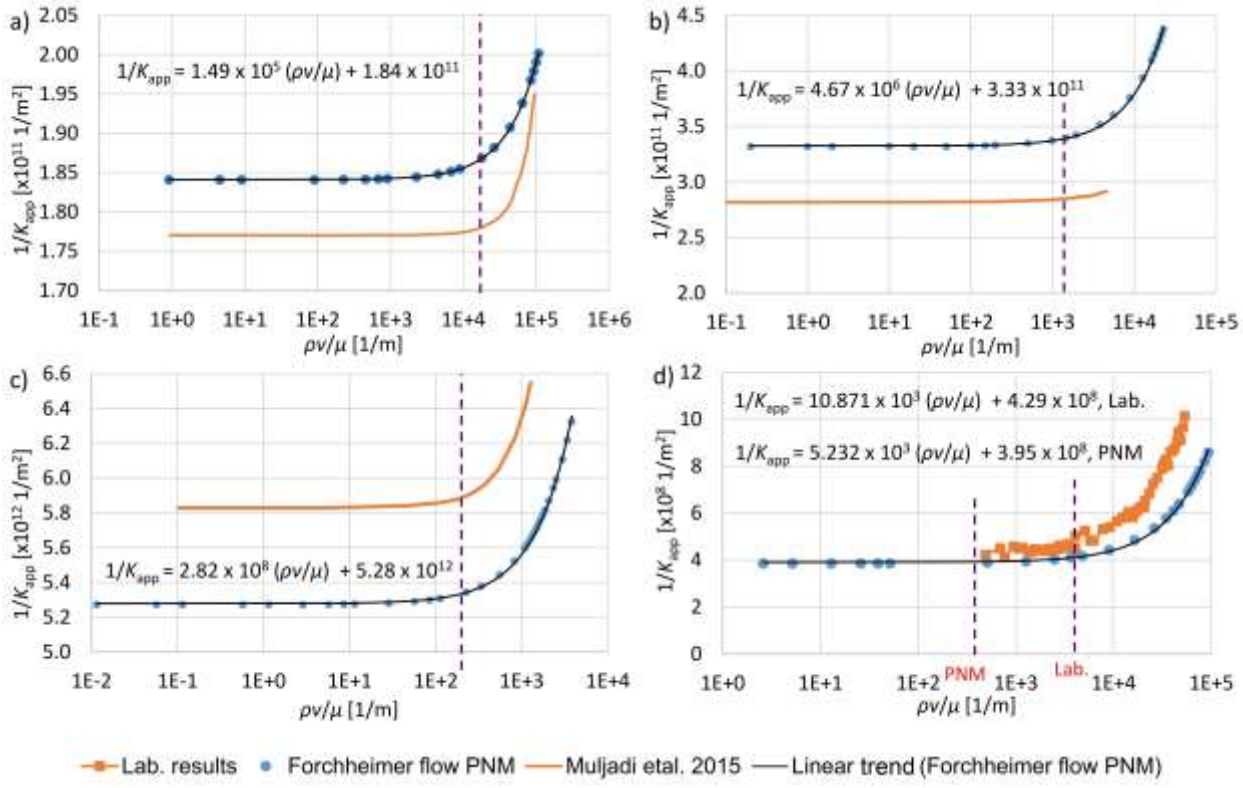

Fig. 5 Forchheimer plot for a) Beadpack, b) Bentheimer c) Estaillades and d) experimental work vs. PNM. The vertical dashed lines represent the onset of non-Darcy flow.

Table 3: The permeability (K_D) and Forchheimer coefficient (β) for the four samples compared to those obtained by Muljadi et al. (2015) and by experiments.

Sample	Image total voxels	$K_D \times 10^{-12}$ (m^2), PNM	$K_D \times 10^{-12}$ (m^2) by Muljadi et al. (2015) or from Lab.	K_D difference [%]	$\beta \times 10^5$ (m^{-1}), PNM	$\beta \times 10^5$ (m^{-1}) by Muljadi et al. (2015) or from Lab.	β difference [%],
Beadpack	300×300×300	5.43	5.57	2.5	1.49	2.57	42
Bentheimer	500×500×500	3.01	3.50	14.0	46.7	20.7	126
Estaillades	500×500×500	0.19	0.170	11.8	2820	6150	54
Packed spheres	758×758×758	2593	2250	15.2	0.0523	0.1087	52

3.4. Onset of non-Darcy flow

Fig. 6 shows the pressure gradient versus superficial velocity at different Reynold's numbers, the figure indicates also the onset of non-Darcy flow. The figure shows a good match with the previous

results obtained by Muljadi et al. (2015) for Beadpack, Bentheimer and Estaillades whilst there are larger discrepancies between PNM and laboratory results. A main cause of these larger discrepancies between PNM and laboratory is that the pores of the packed spheres sample used in the experiments are significantly larger than the other three samples. When a fluid enters a pore, its velocity profile is more likely to be uniform. The fluid then travels a specific distance, known as the entrance length (L_h), until its velocity profile becomes fully developed, i.e. parabolic velocity profile in case of pores with circular cross-section. In the entrance length, the friction between the pore walls and the fluid is higher compared to fully developed flow, and the Hagen–Poiseuille equation is not valid. For laminar flow, L_h is a function of Reynold's number and the pore diameter. It can be estimated as $L_h \cong 0.05\, Re\, D_{pore}$ (Çengel & Cimbala, 2006), where *Re* is the pore Reynold's number and D_{pore} is the pore diameter which is considered as the characteristic length of the pore. For small pores, *Re* is low and L_h is small and can be neglected compared to the total pore length. For that reason, the flow in the majority of pores in the packed spheres sample is a developing flow, i.e. the pore diameters are large and their lengths are not sufficiently long for a fully developed flow to be achieved. This causes an underestimation of the friction factor of each pore in the sample if Hagen–Poiseuille equation is used. This explains why the pressure losses obtained by PNM are less than those obtained in the lab (Fig. 6d).

By estimating the average values of the entrance region (L_h) for all pore throats in the four samples within the applied ranges of pressure gradients, it was found that L_h increases when the applied pressure gradient increases. At the maximum applied pressure gradients, the average values for L_h as a percentage of the average pore throats length were equal to 29%, 11% and 3% for the Beadpack, Bentheimer, and Estaillades, respectively. For the packed spheres sample, at the maximum applied pressure gradients, the average value of L_h, as a percentage of the average pore throats length, reached 374%, which means that the pore lengths are very short and even shorter than L_h. This demonstrates that the PNM approach has limitations and the proposed set of equations cannot be applied for coarse media with large pores.

Another possible reason for the discrepancy between the predicted results and those achieved in the laboratory or through direct numerical simulations presented by Muljadi et al., (2015) is the simplification that was implemented by PNM to describe the geometry of the samples. Also, the mesh size used by Muljadi et al., (2015) may have effects on the accuracy of their results.

According to the Forchheimer equation, the fluid velocity at any pressure gradient is a function of two parameters (K_D and β) which are dependent on the geometry of the porous samples. The superficial velocities calculated using the PNM at the onset of non-Darcy flow are 0.018, 0.001, 0.0001 and 0.0005 m/s for Beadpack, Bentheimer, Estaillades and packed spheres (d_{avg} = 1.84 mm) sample respectively, while the corresponding values presented in Muljadi et al. (2015) and measured in the lab are 0.0279, 0.0014, 0.000227, and 0.004 m/s, see Table 4. It is noticeable that the onset of non-Darcy flow by PNM is in a good match with that obtained by Muljadi et al. (2015), but one order of magnitude lower than the values obtained from experimental measurements which is attributed to the large pore sizes for packed spheres sample and the large entrance length of its pores are explained earlier. In general, it is noticeable that the onset of non-Darcy flow occurs earlier, at lower velocities, when the medium has higher degree of heterogeneity. This is due to a reduction in the effective area for fluid flow in heterogeneous media, as shown in Section 3.5.

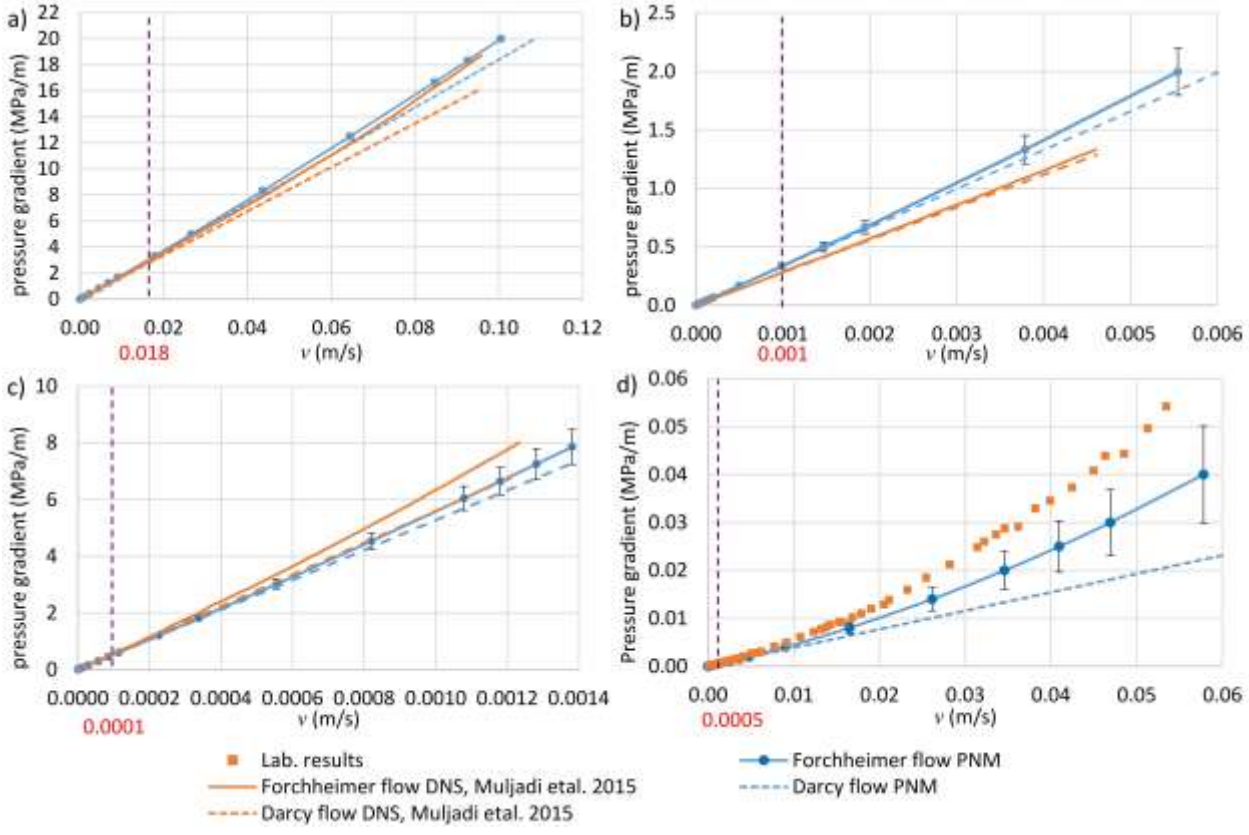

Fig. 6 The pressure gradient versus superficial velocity for both linear Darcy flow and nonlinear Forchheimer flow compared to the results by Muljadi et al. (2015) and laboratory measurements; a) is Beadpack, b) is Bentheimer, c) is Estaillades and d) is the packed spheres sample. The error bars show the difference between the pressure gradient (at specific velocity values) for the

Forchheimer flow case and the corresponding values obtained either by Muljadi et al. (2015) or via experimental measurements.

Considering the dimensionless apparent permeability (K^*) as

$$K^* = \frac{K_{app}}{K_D} \tag{15}$$

and following the same definition for the onset of non-Darcy flow in Section 2.2.2., from equations 1 and 3, the onset of non-Darcy flow can be determined when K^* is equal to 0.99 in Figs. 7 and 8. The predicted superficial velocities and Reynold's number values for the onset of non-Darcy flow and the corresponding values obtained either in Muljadi et al. (2015) work or in the laboratory are shown in Table 4.

In Fig. 7 and Fig. 8, the dimensionless apparent permeability (K^*) is plotted against Re_K and Re_L while using the same characteristic lengths (L_{charc}) used in Muljadi et al. (2015). PNM curves in Fig. 7 and Fig. 8 have similar trends to those in Muljadi et al. (2015) and in the laboratory, but a better match is obtained, especially for Estaillades, in Fig. 7 when Re_K is used instead of Re_L. According to equations 3, 8, 9 and 15 this mismatch is attributed either to the change in superficial velocities or pressure losses in both studies. Therefore, these discrepancies are attributed to the difference between PNM Darcy flow and Forchheimer flow curves in Fig. 6 compared to the difference between the two curves in Muljadi et al. (2015) or in the experimental results. Fig. 7 and Fig. 8 also confirm that the onset of non-Darcy flow occurs earlier, at low Reynold's number, in highly heterogenous media as in the case of Estaillades carbonate. After determining the non-Darcy coefficients (β) for each sample (as shown in Section 3.3), and when the dimensionless apparent permeability (K^*) is plotted versus Forchheimer number $\left(F_o = \frac{K_D\,\beta\,\rho\,V}{\mu}\right)$ in Fig. 9, the curves of all the samples coincide. This unique relationship can be derived mathematically from the Forchheimer Equation (Ruth & Ma, 1992; Ruth & Ma, 1993). In petrophysics, the relationship shown in Fig. 9 can be used to predict the apparent permeability for media with known K_D and β, without the need to perform laboratory experiments at different flow rates. K_D and β can be determined using literature data or empirical relationships such as those proposed by Kozeny (1927), Carman (1937), Ergun (1952), and Janicek and Katz (1955). In Fig. 9, the onset of non-Darcy flow occurs when $K^* = 0.99$, and this corresponds to $F_o \approx 0.01$ for all PNM simulations

and $F_o = 0.1$ for experimental results. These F_o values are in agreement with the range (0.01-0.1) proposed by Andrade et al. (1999).

It is importance to take into consideration the non-Darcy coefficient (β) when determining the onset on non-Darcy flow for different media. For that reason, in Fig. 10, the pressure gradient is plotted versus Forchheimer number, as this is a better comparison tool for follow up studies. The resulting plots are straight lines as expected according to Forchheimer equation (Equation 2). The onset of non-Darcy flow shown in the figure is determined using the superficial velocity at K^* = 0.99.

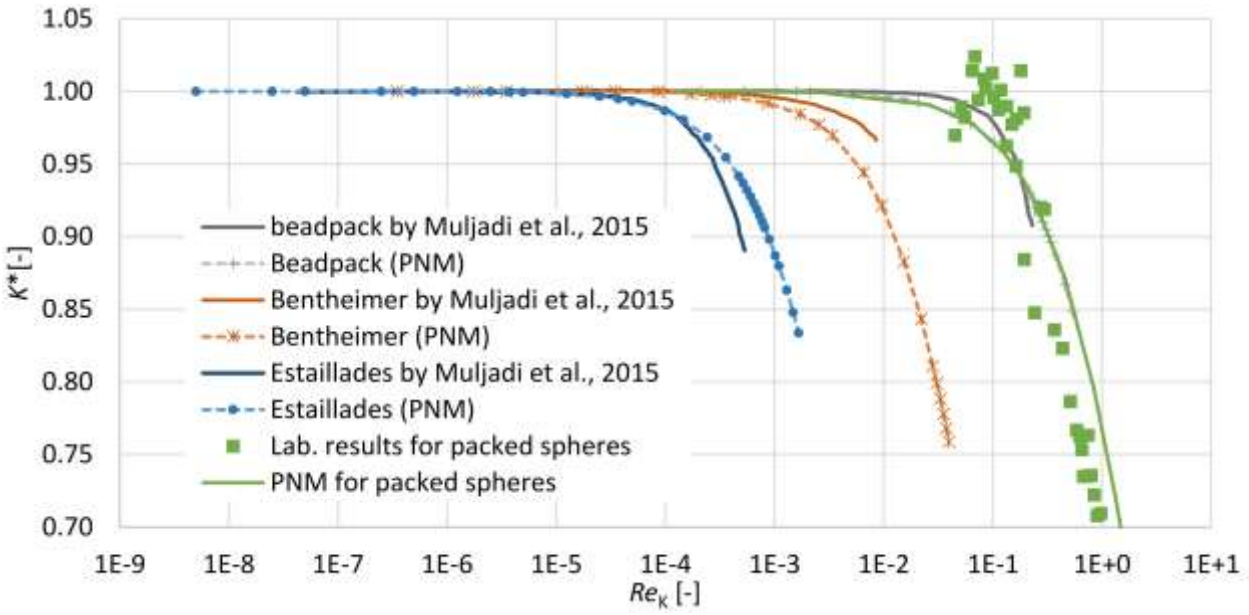

Fig. 7 The dimensionless permeability K^* versus Re_K (Equation 9), compared to the results from Muljadi et al. (2015) and experiments.

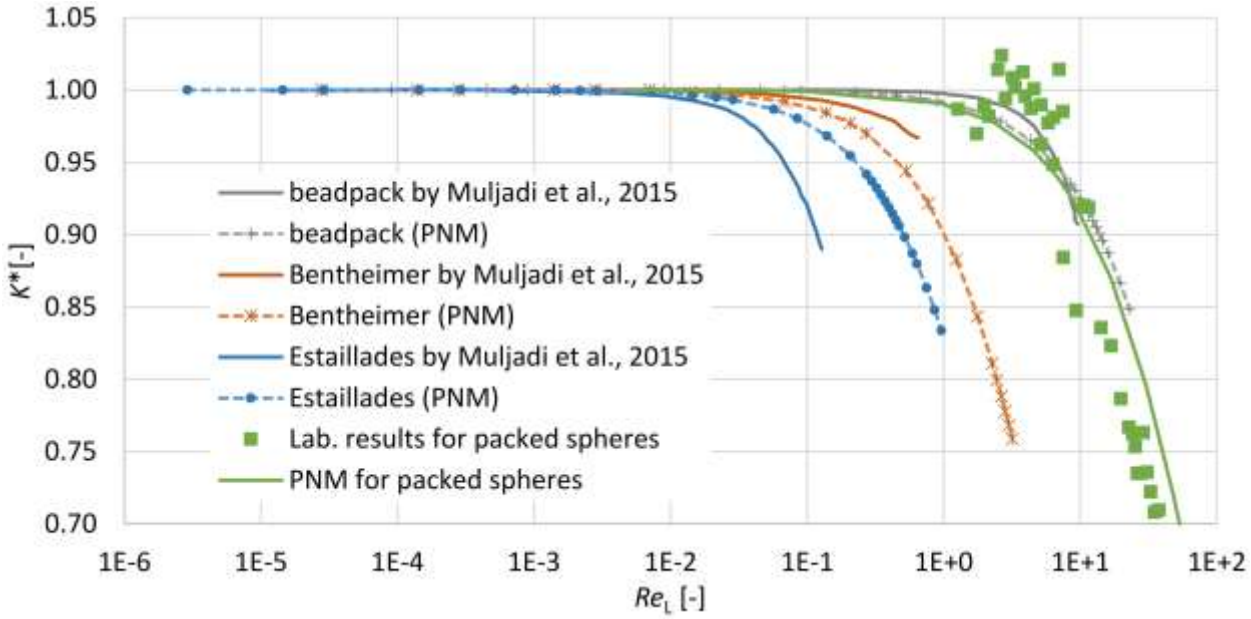

Fig. 8 The dimensionless permeability K^* versus Re_L (Equation 8), compared to the results from Muljadi et al. (2015) and experiments.

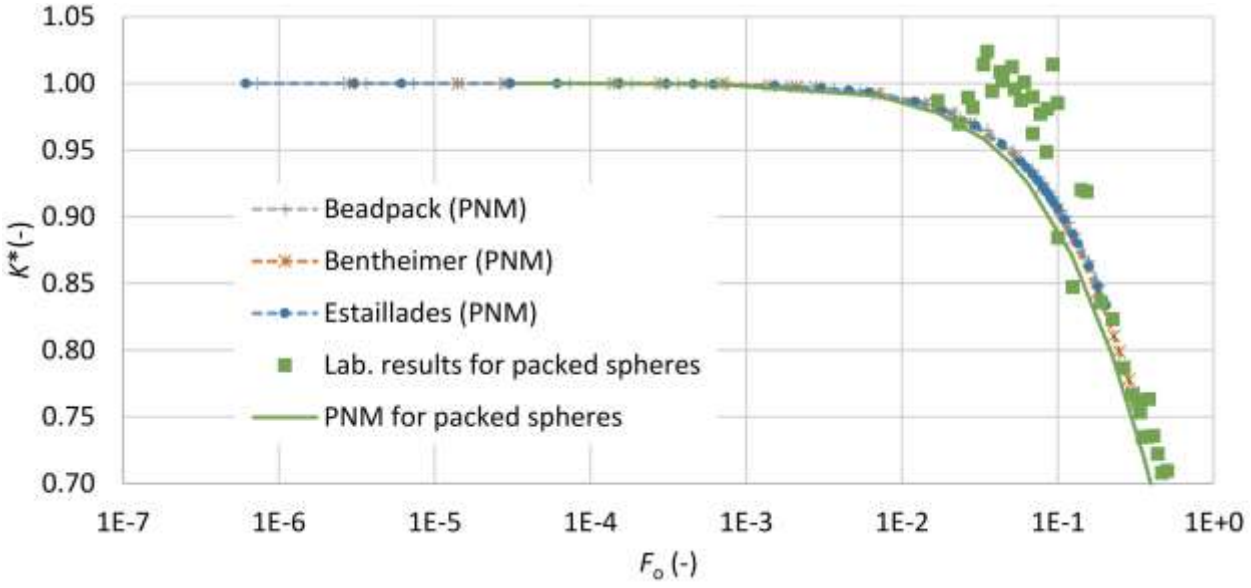

Fig. 9 The dimensionless permeability K^* versus F_o, compared to the results from experiments.

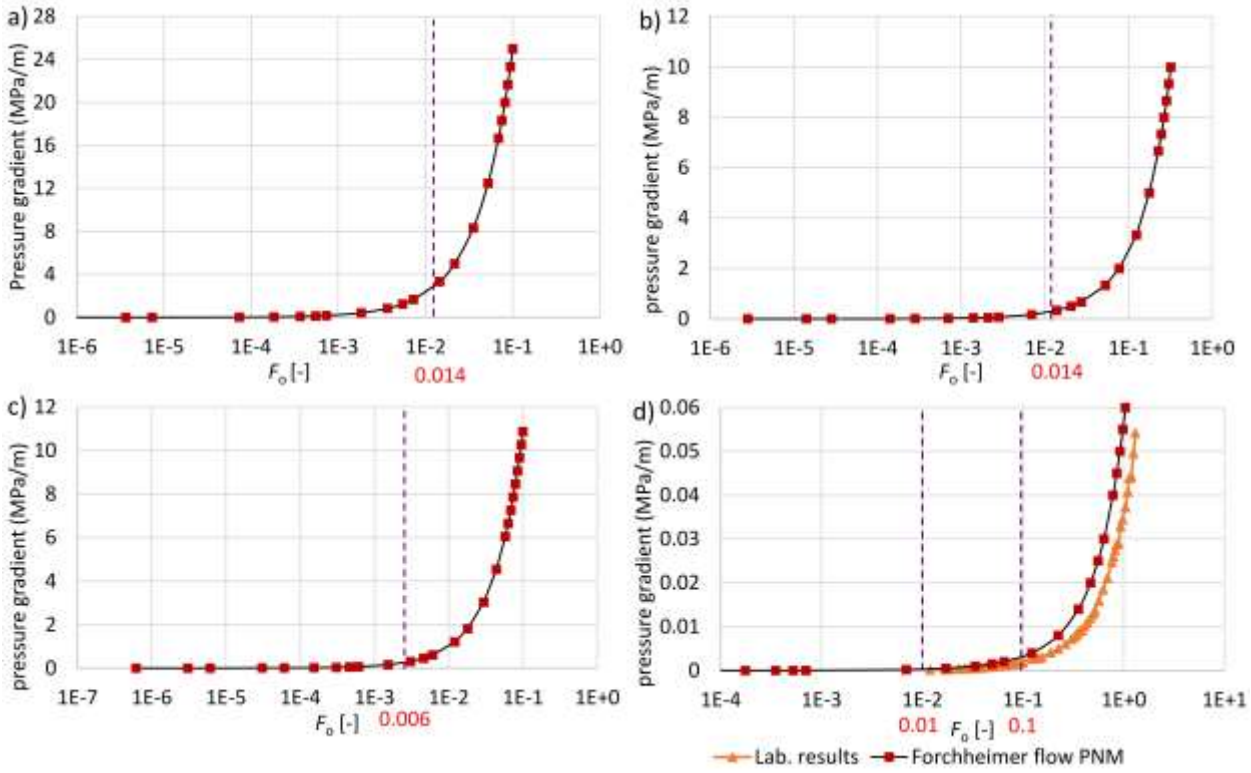

Fig. 10 The pressure gradient versus Forchheimer number (F_o); a) Beadpack, b) Bentheimer c) Estaillades and d) glass-bead packing experiments vs. pore-network modelling results.

Table 4: Reynold's number and superficial velocity values for the onset of non-Darcy flow.

Sample	Onset of non-Darcy flow (pore-network modelling)			Onset of non-Darcy flow obtained by Muljadi et al. (2015) or in the experiments.			Difference [%],		
	v (mm/s)	Re_K	Re_L	v (mm/s)	Re_K	Re_L	v (mm/s)	Re_K	Re_L
Beadpack	17.83	4.15×10^{-2}	1.78	27.9	6.64×10^{-2}	2.79	36	38	36
Bentheimer	0.99	1.72×10^{-3}	0.14	1.4	2.64×10^{-3}	0.196	29	3	29
Estaillades	0.11	4.79×10^{-5}	0.028	0.227	9.4×10^{-5}	0.023	52	5	22
Packed spheres	0.51	2.60×10^{-2}	0.94	4.09	1.94×10^{-1}	7.54	88	87	88

(d_{avg}=1.84 mm)									

511

512 **3.5. Effect of heterogeneity on Pressure distribution**

513 One of the advantages of the pore-network modelling approach is that it provides a detailed
514 overview of the pressure field at the pore-scale as presented in Fig. 11. Fig. 11 shows the pressure
515 value at each pore body versus distance (X) along the flow direction when applying 10000 Pascal
516 pressure drop. The 3D pressure distribution at each pore body is shown at the top right corner for
517 each sub-figure. The dotted black curve represents the average pressure value at any cross-section
518 perpendicular on the flow direction. Inspection of Fig. 11 shows that for the media with low degree
519 of heterogeneity, i.e. beadpack, Bentheimer and packed spheres, there is a regular change of
520 pressure over distance. At any vertical cross-section perpendicular to the flow direction, the
521 maximum pressure variation between pores remains within 25% of the overall pressure drop in the
522 case of beadpack, 10% in the packed spheres and 45% in the Bentheimer. Nevertheless, for highly
523 heterogeneous media, Estaillades, the pressure variation between pores at one cross-section may
524 extend up to 98% of the overall pressure drop. This is mainly caused by the medium heterogeneity
525 that creates some stagnant zones with low pressure values next to the zones with high pressure.
526 The pressure distribution in Fig. 11c shows that the sample is composed of several zones, poorly
527 connected to each other. Therefore, the pressure values within each zone are nearly equal and are
528 significantly different from the pressure values of other zones. Consequently, the velocity
529 distribution within the sample ranges from low in stagnant zones to high at the connection between
530 zones where the inertial effects can be observed even at low pressure gradients.

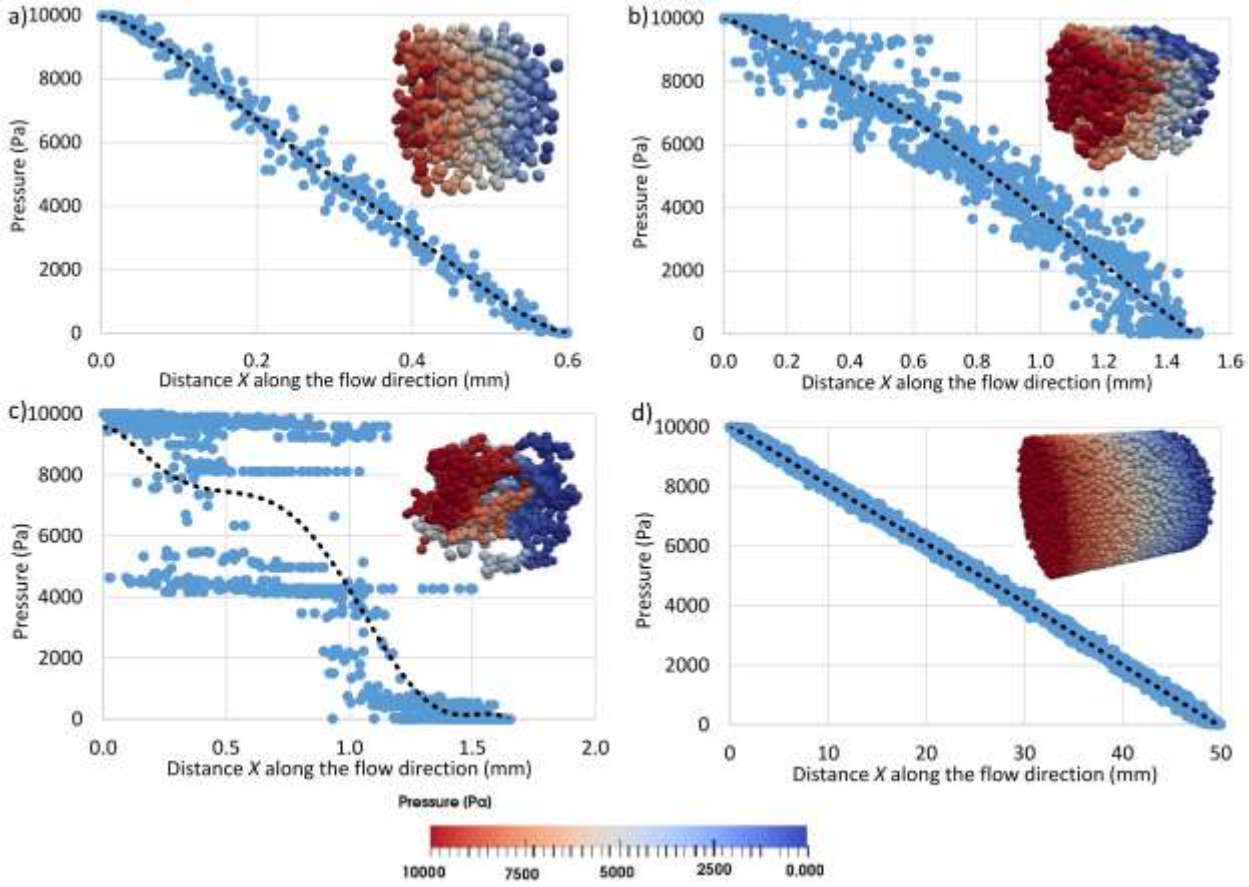

Fig. 11 Pressure values at each pore body vs. distance (*X*) along the flow direction when applying 10000 Pascal pressure drop; a) Beadpack, b) Bentheimer, c) Estaillades and d) Packed spheres. The 3D pressure distribution at each pore body is shown at the top right corner of each sub-figure. The dotted black curve represents the average pressure value at any cross-section perpendicular on the flow direction. The flow direction is from left to right.

3.6. Friction factor

Similar to Hagen–Poiseuille equation (Hagen, 1839; Poiseuille, 1841) for laminar flow through pipes, Moody chart (Moody, 1944) is the most widely used chart for designing flow through pipes in all flow regimes. It is used to estimate the dimensionless friction factor (*f*) of a pipe at specific Reynold's number, and from this friction factor, the pressure needed to pass the flow at specific rate through the pipe can be determined. Thinking of porous media as a group of connected pipes, (Carman, 1937) developed a similar chart that relates the dimensionless friction factor to Reynold's number for porous media in all possible flow regimes (Holdich, 2002). This friction factor can be used to evaluate the medium resistance to flow, or in other words, it can be used to

estimate the pressure needed to pass flow at a specific rate through the porous medium within any flow regime (Hlushkou & Tallarek, 2006).

The friction factor (f) in porous media can be determined by neglecting the small difference between K_D and K_F, then Equation 2 can be rewritten as $f = \frac{1}{F_o} + 1$, where $f = \frac{\Delta P}{L\beta\rho v^2}$ and $F_o = \frac{K_D\beta\rho v}{\mu}$ (Macdonald et al., 1979; Macedo et al., 2001; Pamuk & Özdemir, 2012). Fig. 12 shows that the friction between the medium particles and the fluid decreases with increasing the Forchheimer number, i.e. when the fluid velocity increases. Friction factor and Forchheimer number predictions for all samples are in excellent agreement with each other and in agreement with the experimentally measured values. This agreement is because all the parameters (f, K_D and β) used to develop the figure are predicted from Forchheimer equation. However, this is not the case when the friction factor is plotted versus Reynold's number (not presented), and this shows that Forchheimer number is a better dimensionless parameter that can be used to describe flow through porous media. The resulting friction factor versus Forchheimer number curve is a unique relationship that agrees very well to the results presented by Geertsma (1974) and can be used for all samples regardless of its degree of heterogeneity.

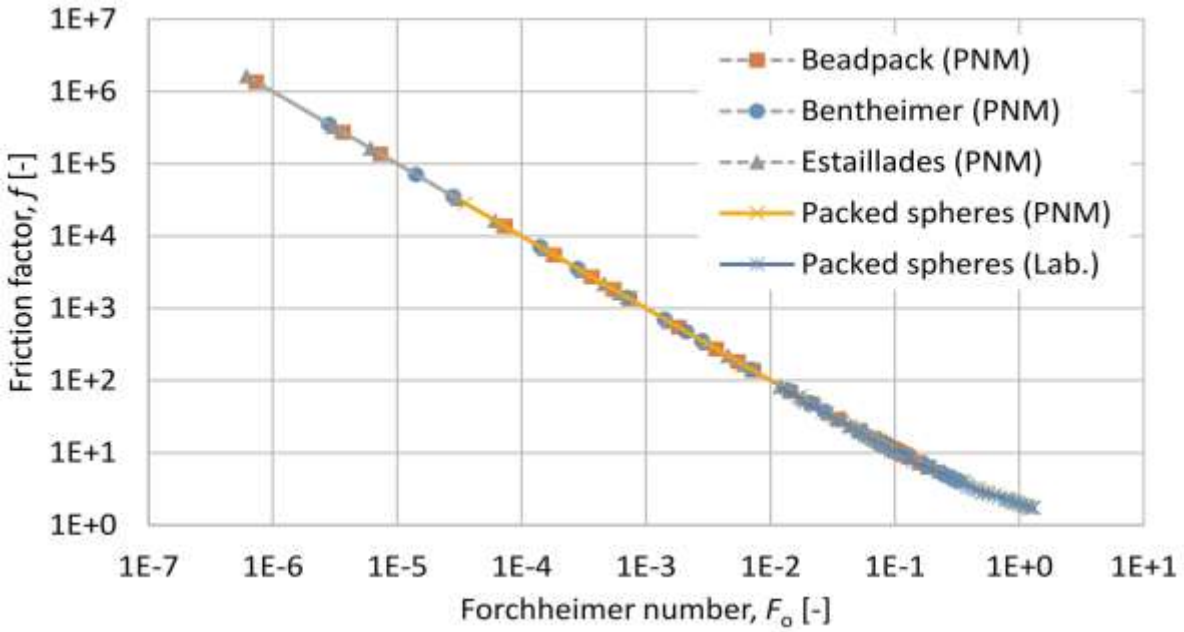

Fig. 12 The medium friction factor (f) versus Forchheimer number (F_o).

3.7. Tortuosity

Wang et al. (1999) defined tortuosity in isotropic media as

$$\tau = \frac{\hat{L}}{\tilde{L}_e} \tag{16}$$

where $\hat{L}$ is the average streamwise flow path or the actual distance including any encountered curves between two points and $\tilde{L}_{\mathrm{e}}$ is the straight distance between these two points. Other authors define tortuosity as the square of this ratio (Dullien, 1992). Thauvin and Mohanty (1998) and Wang et al. (1999) investigated the effect of tortuosity on the non-Darcy coefficient and concluded that its effect is negligible. As it is difficult to obtain tortuosity either experimentally or numerically, Muljadi et al. (2015) used the method proposed by Duda et al. (2011) and Koponen et al. (1996) to obtain tortuosity from the fluid velocity field without the need to determine flow paths as follows:

$$\tau = \frac{\langle |v_{inters}| \rangle}{\langle v_x \rangle} \geq 1 \tag{17}$$

where $\langle |v_{\mathrm{inters}}| \rangle$ is the average magnitude of interstitial velocity over the entire volume and $\langle v_x \rangle$ is the volumetric average of its component along the macroscopic flow direction.

In the proposed PN model, the discharge through each pore throat can be easily determined after solving the pressure value at each node, then the velocity of flow in each pore throat can be determined by dividing the discharge value in each pore throat by the cross-sectional area of that throat. The velocity through the connected pore bodies can be determined by dividing the pore throat discharge by the cross-sectional area of the pore body as well. Then the overall average fluid velocity ($v_{i-j,tot}$) through the pore throat and the two connected pore bodies can be estimated as the length harmonic average of the velocities (Equation 18, Fig. 1).

$$\frac{L_{i-j,tot}}{v_{i-j,tot}} = \frac{L_i}{v_i} + \frac{L_{i-j}}{v_{i-j}} + \frac{L_j}{v_j} \tag{18}$$

where $v_{i\text{-}j}$ is the velocity of flow through the pore throat that connects the two pore bodies *i* and *j*, v_i and v_j are the fluid velocity through the pore bodies *i* and *j*.

Finally, the volumetric average interstitial velocity $\langle |v_{inters}| \rangle$ can be obtained as

$$\langle |v_{inters}| \rangle = \frac{\sum (v_{i-j,tot}\, a_{i-j})}{\sum a_{i-j}} \tag{19}$$

Similarly, v_x for each pore throat can be estimated as the *X*-component, along the macroscopic flow direction, corresponding to each $v_{i-j,tot}$. Then, $\langle v_x \rangle$ can be obtained by replacing $v_{i-j,tot}$ by

588 v_x in Equation 19. Fig. 13 shows that tortuosity increases slightly with increasing the Reynold's
589 number, this is due to the increase in velocities and the possible occurrence of some eddies. All
590 samples in Fig. 13 have a trend similar to that obtained by Muljadi et al. (2015) and Chukwudozie
591 et al. (2012) and are in agreement (varying with in less than 8%) with the values obtained by
592 Muljadi et al. (2015). It is noticeable that in Fig. 13c, the increasing trend of τ is delayed compared
593 to Muljadi et al. (2015), this is attributed to some discrepancies in predicting the flow velocities
594 and pressures loss (as in Fig. 6c) for Estaillades. Due to the heterogeneity of Estaillades, its
595 tortuosity is larger than other samples. This is due to the poor connectivity between different zones
596 in the sample, as in Section 3.5., so each fluid particle may need to travel a longer path.

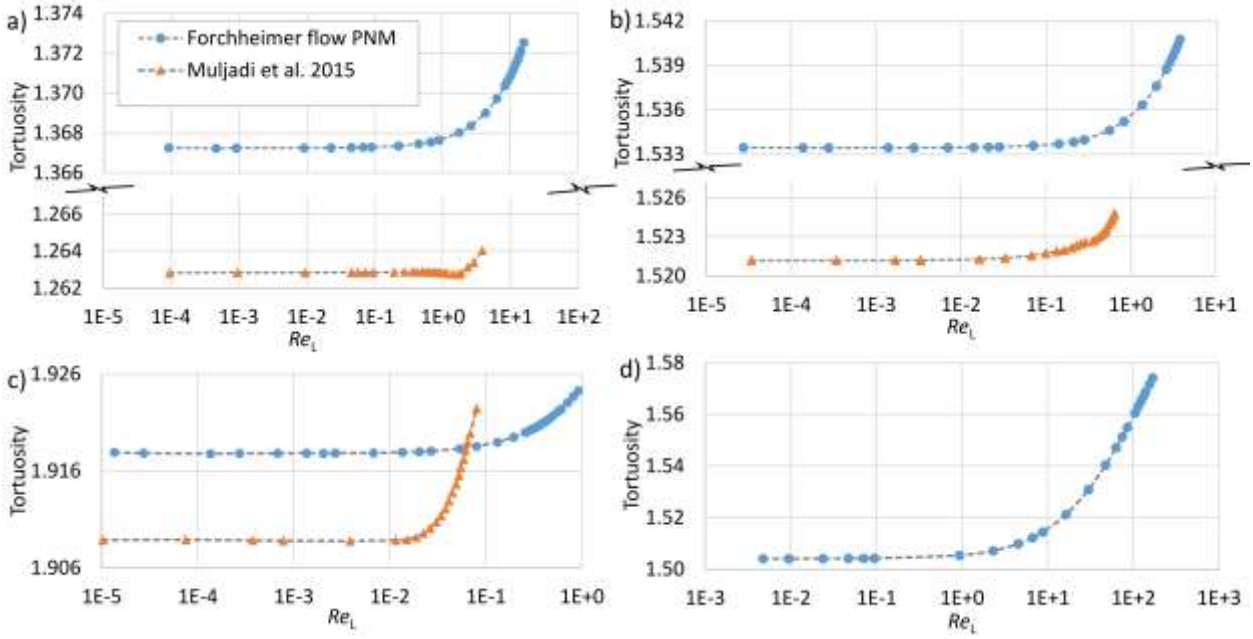

597
598

599 **Fig. 13** Tortuosity versus Re_L for; a) Beadpack, b) is Bentheimer, c) Estaillades and d) Packed
600 sphere samples.

601 ## 4. Conclusion

602 In this work, Darcy permeability, apparent permeability, non-Darcy coefficient and tortuosity were
603 estimated for four porous samples (beadpack, Bentheimer sandstone, Estaillades carbonate and
604 packed spheres) with different degrees of heterogeneity using pore-network modelling and
605 applying the Forchheimer equation. The proposed model overcomes most of the limitations in
606 previous studies that used pore-network modelling to simulate non-Darcy flow; limited
607 coordination number, 2D simulations only, inaccuracy of some equations, limitation regarding the

608 use of regular structured networks only and lack of calibration. In addition, the onset of non-Darcy
609 flow was fully investigated in detail for all samples.

610 Based on findings of this research, it is concluded that Forchheimer number (F_o), instead of the
611 permeability-based Reynold's number (Re_K) or standard Reynold's number (Re_L), can be used as
612 a criterion to determine the onset of non-Darcy flow. This is because Forchheimer number
613 accounts for Darcy permeability, the Forchheimer coefficient and the medium degree of
614 heterogeneity. The onset of non-Darcy flow, determined at K^*=0.99 and using Re_K, is highly
615 dependent on the degree of heterogeneity. For Bentheimer sandstone the onset of non-Darcy flow
616 is one order of magnitude smaller than in the case of beadpack, and for Estaillades the onset of
617 non-Darcy flow is three orders of magnitudes smaller than in the case of beadpack. Nevertheless,
618 the Forchheimer number values for the onset of non-Darcy flow for the four samples ranged from
619 0.01 to 0.1 and this is in agreement with Andrade et al. (1999).

620 The Darcy Permeabilities (K_D) and Forchheimer coefficients (β) for all samples are in a good
621 agreement (varying within 15.2% and 54% respectively) with the values obtained either in the
622 laboratory or by Muljadi et al. (2015) for the same samples, except in the case of Bentheimer, its
623 β value varied 126%.

624 The medium friction factor is a good feature that can be used to calculate the pressure gradient at
625 different velocities for different flow regimes, regardless the heterogeneity of the medium, if the
626 Darcy permeability and Forchheimer coefficient are known. It was found that the medium friction
627 coefficient decreases when the fluid velocity increases. Following the Forchheimer equation, the
628 medium friction factor versus Forchheimer number curve is identical for all media regardless of
629 their degree of heterogeneity. Tortuosity was found to increase slightly with increasing the flow
630 velocity, in all samples.

631 For highly heterogeneous media, i.e. Estaillades, the pressure variation between pores at one cross-
632 section (perpendicular to the flow direction) may extend up to 98% of the overall pressure drop.
633 This is mainly caused by the medium heterogeneity that creates some stagnant zones with low
634 pressure values next to other zones with high pressure values.

635 The pore-network modelling approach has been shown to be computationally more efficient in
636 comparison with direct flow simulations and could dramatically reduce the running time from few

hours (3 hours and 37 minutes for the Estaillades model in Muljadi et al. (2015) work) using 16 parallel computer nodes to less than one minute using a standard PC, but it is still relatively memory demanding when a large number of pore bodies is used, especially for non-linear flow simulations. For instance, a pore-network with 120,000 pore bodies requires 185 GB Ram. Nevertheless, in terms of pore geometries, direct numerical simulation is believed to be more accurate than pore-network modelling which simplifies the irregular pore shapes into pores with simple geometries for which the analytical flow equations can be applied.

Acknowledgment

We acknowledge the fund given to the first author from the Newton-Mosharafa program as a collaboration between the British Council and the Egyptian Ministry of Higher Education. Dr Bagus Muljadi and Dr Ali Raeini are acknowledged for providing part of the CT-images used in this study. The anonymous reviewers are acknowledged for their constructive comments.

References

Abdelall, F. F., Hahn, G., Ghiaasiaan, S. M., Abdel-Khalik, S. I., Jeter, S. S., Yoda, M., & Sadowski, D. L. (2005). Pressure drop caused by abrupt flow area changes in small channels. *Experimental Thermal and Fluid Science, 29*(4), 425-434. doi:https://doi.org/10.1016/j.expthermflusci.2004.05.001

Akhlaghi Amiri, H. A., & Hamouda, A. A. (2013). Evaluation of level set and phase field methods in modeling two phase flow with viscosity contrast through dual-permeability porous medium. *International Journal of Multiphase Flow, 52*, 22-34. doi:http://dx.doi.org/10.1016/j.ijmultiphaseflow.2012.12.006

Al-Raoush, R., Thompson, K., & Willson, C. S. (2003). Comparison of Network Generation Techniques for Unconsolidated Porous Media. *Soil Science Society of America Journal, 67*(6), 1687-1700. doi:10.2136/sssaj2003.1687

Alfonsi, G. (2011). On Direct Numerical Simulation of Turbulent Flows. *Applied Mechanics Reviews, 64*(2), 020802-020802-020833. doi:10.1115/1.4005282

Aly, A. M., & Asai, M. (2015). Modelling of Non-Darcy Flows through Porous Media Using Extended Incompressible Smoothed Particle Hydrodynamics. *Numerical Heat Transfer, Part B: Fundamentals, 67*(3), 255-279. doi:10.1080/10407790.2014.955772

Andrade, J. S., Costa, U. M. S., Almeida, M. P., Makse, H. A., & Stanley, H. E. (1999). Inertial Effects on Fluid Flow through Disordered Porous Media. *Physical Review Letters, 82*(26), 5249-5252. doi:10.1103/PhysRevLett.82.5249

675 Aziz, R., Joekar-Niasar, V., & Martinez-Ferrer, P. (2018). Pore-scale insights into transport and mixing in
676 steady-state two-phase flow in porous media. *International Journal of Multiphase Flow, 109*, 51-
677 62. doi:https://doi.org/10.1016/j.ijmultiphaseflow.2018.07.006
678
679 Babaei, M., & Joekar-Niasar, V. (2016). A transport phase diagram for pore-level correlated porous
680 media. *Advances in Water Resources, 92*, 23-29.
681 doi:http://dx.doi.org/10.1016/j.advwatres.2016.03.014
682
683 Balhoff, M. T., & Wheeler, M. F. (2009). A Predictive Pore-Scale Model for Non-Darcy Flow in Porous
684 Media. *SPE Journal, 14*(03), 579-587.
685
686 Bandara, U. C., Tartakovsky, A. M., Oostrom, M., Palmer, B. J., Grate, J., & Zhang, C. (2013). Smoothed
687 particle hydrodynamics pore-scale simulations of unstable immiscible flow in porous media.
688 *Advances in Water Resources, 62, Part C*, 356-369.
689 doi:http://dx.doi.org/10.1016/j.advwatres.2013.09.014
690
691 Bear, J. (1972). *Dynamics of Fluids in Porous Media*. Elsevier, New York.
692
693 Belhaj, H. A., Agha, K. R., Nouri, A. M., Butt, S. D., Vaziri, H. H., & Islam, M. R. (2003). *Numerical Modeling*
694 *of Forchheimer's Equation to Describe Darcy and Non-Darcy Flow in Porous Media*. Paper
695 presented at the SPE Asia Pacific Oil and Gas Conference and Exhibition, Jakarta, Indonesia.
696 https://doi.org/10.2118/80440-MS
697
698 Bijeljic, B., & Blunt, M. J. (2007). Pore-scale modeling of transverse dispersion in porous media. *Water*
699 *Resources Research, 43*(12), W12S11. doi:10.1029/2006WR005700
700
701 Bijeljic, B., Mostaghimi, P., & Blunt, M. J. (2013a). Insights into non-Fickian solute transport in
702 carbonates. *Water Resources Research, 49*(5), 2714-2728. doi:10.1002/wrcr.20238
703
704 Bijeljic, B., Muggeridge, A. H., & Blunt, M. J. (2004). Pore-scale modeling of longitudinal dispersion.
705 *Water Resources Research, 40*(11), W11501. doi:10.1029/2004WR003567
706
707 Bijeljic, B., Raeini, A., Mostaghimi, P., & Blunt, M. J. (2013b). Predictions of non-Fickian solute transport
708 in different classes of porous media using direct simulation on pore-scale images. *Physical*
709 *Review E, 87*(1), 013011.
710
711 Bird, R. B., Stewart, W. E., & Lightfoot, E. N. (1960). *Transport phenomena. New York: John Wiley and*
712 *Sons.*
713
714 Bird, R. B., Stewart, W. E., & Lightfoot, E. N. (1961). Transport phenomena, John Wiley and Sons, Inc.,
715 New York (1960). 780 pages. $11.50. *AIChE Journal, 7*(2), 5J-6J. doi:10.1002/aic.690070245
716
717 Blunt, M. J., Bijeljic, B., Dong, H., Gharbi, O., Iglauer, S., Mostaghimi, P., Paluszny, A., & Pentland, C.
718 (2013). Pore-scale imaging and modelling. *Advances in Water Resources, 51*, 197-216.
719 doi:http://dx.doi.org/10.1016/j.advwatres.2012.03.003
720
721 Bryant, S., & Blunt, M. (1992). Prediction of relative permeability in simple porous media. *Physical*
722 *Review A, 46*(4), 2004-2011.

Bryant, S. L., Mellor, D. W., & Cade, C. A. (1993). Physically representative network models of transport in porous media. *AIChE Journal, 39*(3), 387-396. doi:10.1002/aic.690390303

Carman, P. C. (1937). Fluid flow through granular beds. *Chemical Engineering Research and Design, 75*, S32-S48. doi:https://doi.org/10.1016/S0263-8762(97)80003-2

Celia, M. A., Reeves, P. C., & Ferrand, L. A. (1995). Recent advances in pore scale models for multiphase flow in porous media. *Reviews of Geophysics, 33*(S2), 1049-1057. doi:10.1029/95RG00248

Çengel, Y. A., & Cimbala, J. M. (2006). *Fluid mechanics: Fundamentals and applications.* Boston: McGraw-HillHigher Education.

Chukwudozie, C. P., Tyagi, M., Sears, S. O., & White, C. D. (2012). Prediction of Non-Darcy Coefficients for Inertial Flows Through the Castlegate Sandstone Using Image-Based Modeling. *Transport in Porous Media, 95*(3), 563-580. doi:10.1007/s11242-012-0062-5

Comiti, J., Sabiri, N. E., & Montillet, A. (2000). Experimental characterization of flow regimes in various porous media — III: limit of Darcy's or creeping flow regime for Newtonian and purely viscous non-Newtonian fluids. *Chemical Engineering Science, 55*(15), 3057-3061. doi:http://dx.doi.org/10.1016/S0009-2509(99)00556-4

Crane. (1942). *Flow of fluids through valves, fittings and pipe*. Chicago, III: Crane co.

Darcy, H. (1856). Les Fontaines Publiques de la Vile de Dijon. *Victor Dalmond, Paris.*

Duda, A., Koza, Z., & Matyka, M. (2011). Hydraulic tortuosity in arbitrary porous media flow. *Physical Review E, 84*(3), 036319.

Dullien, F. A. L. (1992). *Porous Media: Fluid Transport and Pore Structure*. San Diego: Academic Press.

Durlofsky, L., & Brady, J. F. (1987). Analysis of the Brinkman equation as a model for flow in porous media. *The Physics of Fluids, 30*(11), 3329-3341. doi:10.1063/1.866465

El-Zehairy, A. A., Lubczynski, M. W., & Gurwin, J. (2018). Interactions of artificial lakes with groundwater applying an integrated MODFLOW solution. *Hydrogeology Journal, 26*(1), 109-132. doi:10.1007/s10040-017-1641-x

Ergun, S. (1952). Fluid Flow through Packed Columns. *Chem. Eng. Prog., 48*, 89–94.

Finney, J. L. (1970). Random packings and the structure of simple liquids. I. The geometry of random close packing. *Proceedings of the Royal Society of London. A. Mathematical and Physical Sciences, 319*(1539), 479-493. doi:doi:10.1098/rspa.1970.0189

Forchheimer, P. (1901). Wasserbewegung durch Boden. *Zeitschrift des Vereins deutscher Ingenieure 45, no. 1: 1782–1788.*

770 Gao, S., Meegoda, J. N., & Hu, L. (2012). Two methods for pore network of porous media. *International*
771 *Journal for Numerical and Analytical Methods in Geomechanics, 36*(18), 1954-1970.
772 doi:10.1002/nag.1134
773
774 Geertsma, J. (1974). Estimating the Coefficient of Inertial Resistance in Fluid Flow Through Porous
775 Media. *Society of Petroleum Engineers Journal, 14*(05), 445-450. doi:10.2118/4706-PA
776
777 Geiger, G. E. (1964). *Sudden contraction losses in single and two-phase flow.* (Ph.D. thesis), University of
778 Pittsburgh, Pittsburgh, PA.
779 Guadagnini, A., Blunt, M. J., Riva, M., & Bijeljic, B. (2014). Statistical Scaling of Geometric Characteristics
780 in Millimeter Scale Natural Porous Media. *Transport in Porous Media, 101*(3), 465-475.
781 doi:10.1007/s11242-013-0254-7
782
783 Guo, H., Wang, L., Yu, J., Ye, F., Ma, C., & Li, Z. (2010). Local resistance of fluid flow across sudden
784 contraction in small channels. *Frontiers of Energy and Power Engineering in China, 4*(2), 149-154.
785 doi:10.1007/s11708-009-0060-7
786
787 Hagen, G. (1839). Ueber die Bewegung des Wassers in engen cylindrischen Röhren. *Annalen der Physik,*
788 *122*(3), 423-442. doi:10.1002/andp.18391220304
789
790 Hlushkou, D., & Tallarek, U. (2006). Transition from creeping via viscous-inertial to turbulent flow in
791 fixed beds. *Journal of Chromatography A, 1126*(1–2), 70-85.
792 doi:https://doi.org/10.1016/j.chroma.2006.06.011
793
794 Holdich, R. G. (2002). *Fundementals of particle technology*. Midland Information Technology and
795 Publishing, Shepshed.
796
797 HSL. (2013). A collection of Fortran codes for large scale scientific computation. *http://www.hsl.rl.ac.uk*.
798
799 Janicek, J., & Katz, D. (1955). Applications of unsteady state gas flow calculations. *In: Proceedings of*
800 *University of Michigan research conference*.
801
802 Joekar-Niasar , V., & Hassanizadeh, S. M. (2012). Analysis of Fundamentals of Two-Phase Flow in Porous
803 Media Using Dynamic Pore-Network Models: A Review. *Critical Reviews in Environmental*
804 *Science and Technology, 42*(18), 1895-1976. doi:10.1080/10643389.2011.574101
805
806 Joekar-Niasar, V., Prodanović, M., Wildenschild, D., & Hassanizadeh, S. M. (2010). Network model
807 investigation of interfacial area, capillary pressure and saturation relationships in granular
808 porous media. *Water Resources Research, 46*(6), W06526. doi:10.1029/2009WR008585
809
810 Joekar Niasar, V., Hassanizadeh, S. M., Pyrak-Nolte, L. J., & Berentsen, C. (2009). Simulating drainage and
811 imbibition experiments in a high-porosity micromodel using an unstructured pore network
812 model. *Water Resources Research, 45*(2), W02430. doi:10.1029/2007WR006641
813
814 Kays, W. M. (1950). Loss Coefficient for Abrupt Changes in Flow Cross Section with Reynolds Number
815 Flow in Single and Multiple Mube Systems. *Transactions of the American Society of Mechanical*
816 *Engineers, 72*, 1067-1074.
817

Knackstedt, M. A., Sheppard, A. P., & Sahimi, M. (2001). Pore network modelling of two-phase flow in porous rock: the effect of correlated heterogeneity. *Advances in Water Resources, 24*(3–4), 257-277. doi:http://dx.doi.org/10.1016/S0309-1708(00)00057-9

Koponen, A., Kataja, M., & Timonen, J. (1996). Tortuous flow in porous media. *Physical Review E, 54*(1), 406-410.

Kozeny, J. (1927). Über kapillare Leitung des Wassers im Boden. *Akad. Wiss. Wien, 136*, 271-306. doi:citeulike-article-id:4155258

Kuwata, Y., & Suga, K. (2015). Large eddy simulations of pore-scale turbulent flows in porous media by the lattice Boltzmann method. *International Journal of Heat and Fluid Flow, 55*, 143-157. doi:http://dx.doi.org/10.1016/j.ijheatfluidflow.2015.05.015

Lao, H. W., Neeman, H. J., & Papavassiliou, D. V. (2004). A pore network model for the calculation of non-Darcy flow coefficients in fluid flow through porous media. *Chemical Engineering Communications, 191*(10), 1285-1322. doi:10.1080/00986440490464200

Lemley, E. C., Papavassiliou, D. V., & Neeman, H. J. (2007). *Non-Darcy Flow Pore Network Simulation: Development and Validation of a 3D Model.* Paper presented at the ASME/JSME 2007 5th Joint Fluids Engineering Conference.

Liu, X., Civan, F., & Evans, R. D. (1995). Correlation of the Non-Darcy Flow Coefficient. *Journal of Canadian Petroleum Technology, 34*(10), 6. doi:10.2118/95-10-05

Macdonald, I. F., El-Sayed, M. S., Mow, K., & Dullien, F. A. L. (1979). Flow through Porous Media-the Ergun Equation Revisited. *Industrial & Engineering Chemistry Fundamentals, 18*(3), 199-208. doi:10.1021/i160071a001

Macedo, H. H., Costa, U. M. S., & Almeida, M. P. (2001). Turbulent effects on fluid flow through disordered porous media. *Physica A: Statistical Mechanics and its Applications, 299*(3–4), 371-377. doi:http://dx.doi.org/10.1016/S0378-4371(01)00257-6

Mason, G., & Morrow, N. R. (1991). Capillary behavior of a perfectly wetting liquid in irregular triangular tubes. *Journal of Colloid and Interface Science, 141*(1), 262-274. doi:http://dx.doi.org/10.1016/0021-9797(91)90321-X

Moin, P., & Mahesh, K. (1998). DIRECT NUMERICAL SIMULATION: A Tool in Turbulence Research. *Annual Review of Fluid Mechanics, 30*(1), 539-578. doi:10.1146/annurev.fluid.30.1.539

Momen, A. M., Sherif, S. A., & Lear, W. (2016). An Analytical-Numerical Model for Two-Phase Slug Flow through a Sudden Area Change in Microchannels. *Journal of Applied Fluid Mechanics, Vol. 9, No. 4, pp. 1839-1850*.

Moody, L. F. (1944). Friction Factors for Pipe Flow. *Transactions of the American Society of Mechanical Engineers, 66, 671-681*.

Mostaghimi, P., Bijeljic, B., & Blunt, M. (2012). Simulation of Flow and Dispersion on Pore-Space Images. doi:10.2118/135261-PA

Mousavi Nezhad, M., & Javadi, A. A. (2011). Stochastic Finite-Element Approach to Quantify and Reduce Uncertainty in Pollutant Transport Modeling. *Journal of Hazardous, Toxic, and Radioactive Waste, 15*(3), 208-215. doi:doi:10.1061/(ASCE)HZ.1944-8376.0000055

Mousavi Nezhad, M., Javadi, A. A., & Rezania, M. (2011). Modeling of contaminant transport in soils considering the effects of micro- and macro-heterogeneity. *Journal of Hydrology, 404*(3), 332-338. doi:https://doi.org/10.1016/j.jhydrol.2011.05.004

Muljadi, B. P., Blunt, M. J., Raeini, A. Q., & Bijeljic, B. (2015). The impact of porous media heterogeneity on non-Darcy flow behaviour from pore-scale simulation. *Advances in Water Resources*. doi:http://dx.doi.org/10.1016/j.advwatres.2015.05.019

Oostrom, M., Mehmani, Y., Romero-Gomez, P., Tang, Y., Liu, H., Yoon, H., Kang, Q., Joekar-Niasar, V., Balhoff, M. T., Dewers, T., Tartakovsky, G. D., Leist, E. A., Hess, N. J., Perkins, W. A., Rakowski, C. L., Richmond, M. C., Serkowski, J. A., Werth, C. J., Valocchi, A. J., Wietsma, T. W., & Zhang, C. (2016). Pore-scale and continuum simulations of solute transport micromodel benchmark experiments. *Computational Geosciences, 20*(4), 857-879. doi:10.1007/s10596-014-9424-0

Oren, P. E., Bakke, S., & Arntzen, O. J. (1998). Extending Predictive Capabilities to Network Models. doi:10.2118/52052-PA

Pamuk, M. T., & Özdemir, M. (2012). Friction factor, permeability and inertial coefficient of oscillating flow through porous media of packed balls. *Experimental Thermal and Fluid Science, 38*, 134-139. doi:http://dx.doi.org/10.1016/j.expthermflusci.2011.12.002

Patzek, T. W., & Silin, D. B. (2001). Shape Factor and Hydraulic Conductance in Noncircular Capillaries. *Journal of Colloid and Interface Science, 236*(2), 295-304. doi:http://dx.doi.org/10.1006/jcis.2000.7413

Poinsot, T., Candel, S., & Trouvé, A. (1995). Applications of direct numerical simulation to premixed turbulent combustion. *Progress in Energy and Combustion Science, 21*(6), 531-576. doi:https://doi.org/10.1016/0360-1285(95)00011-9

Poiseuille, J. L. M. (1841). Recherches expérimentales sur le mouvement des liquides dans les tubes de très petits diamèstres. *Memoires Presentes par Divers Savants a l Academie Royal de l Institut de France,9: 433-544*.

Prodanović, M., & Bryant, S. L. (2006). A level set method for determining critical curvatures for drainage and imbibition. *Journal of Colloid and Interface Science, 304*(2), 442-458. doi:http://dx.doi.org/10.1016/j.jcis.2006.08.048

Raeini, A. Q., Bijeljic, B., & Blunt, M. J. (2017). Generalized network modeling: Network extraction as a coarse-scale discretization of the void space of porous media. *Physical Review E, 96*(1), 013312. doi:10.1103/PhysRevE.96.013312

913 Raeini, A. Q., Bijeljic, B., & Blunt, M. J. (2018). Generalized network modeling of capillary-dominated
914 two-phase flow. *Physical Review E, 97*(2), 023308. doi:10.1103/PhysRevE.97.023308
915
916 Raeini, A. Q., Blunt, M. J., & Bijeljic, B. (2012). Modelling two-phase flow in porous media at the pore
917 scale using the volume-of-fluid method. *Journal of Computational Physics, 231*(17), 5653-5668.
918 doi:https://doi.org/10.1016/j.jcp.2012.04.011
919
920 Ruth, D., & Ma, H. (1992). On the derivation of the Forchheimer equation by means of the averaging
921 theorem. *Transport in Porous Media, 7*(3), 255-264. doi:10.1007/bf01063962
922
923 Ruth, D. W., & Ma, H. (1993). Numerical analysis of viscous, incompressible flow in a diverging-
924 converging RUC. *Transport in Porous Media, 13*(2), 161-177. doi:10.1007/bf00654408
925
926 Sahimi, M. (2011). Continuum versus Discrete Models. *In Flow and Transport in Porous Media and*
927 *Fractured Rock*.
928
929 Tartakovsky, A. M., Trask, N., Pan, K., Jones, B., Pan, W., & Williams, J. R. (2015). Smoothed particle
930 hydrodynamics and its applications for multiphase flow and reactive transport in porous media.
931 *Computational Geosciences*, 1-28. doi:10.1007/s10596-015-9468-9
932
933 Thauvin, F., & Mohanty, K. K. (1998). Network Modeling of Non-Darcy Flow Through Porous Media.
934 *Transport in Porous Media, 31*(1), 19-37. doi:10.1023/a:1006558926606
935
936 Vafai, K., & Tien, C. L. (1981). Boundary and inertia effects on flow and heat transfer in porous media.
937 *International Journal of Heat and Mass Transfer, 24*(2), 195-203.
938 doi:http://dx.doi.org/10.1016/0017-9310(81)90027-2
939
940 Valvatne, P. H., & Blunt, M. J. (2004). Predictive pore-scale modeling of two-phase flow in mixed wet
941 media. *Water Resources Research, 40*(7), W07406. doi:10.1029/2003WR002627
942
943 Wang, X., Thauvin, F., & Mohanty, K. K. (1999). Non-Darcy flow through anisotropic porous media.
944 *Chemical Engineering Science, 54*(12), 1859-1869. doi:http://dx.doi.org/10.1016/S0009-
945 2509(99)00018-4
946
947 Wilkinson, D. (1984). Percolation model of immiscible displacement in the presence of buoyancy forces.
948 *Physical Review A, 30*(1), 520-531.
949
950 Wu, J., Hu, D., Li, W., & Cai, X. I. N. (2016). A review on non-Darcy flow-Forchheimer equation, Hydraulic
951 radius model, fractal model and experiment. *Fractals, 24*(02), 1630001.
952 doi:10.1142/S0218348X16300014
953
954 Xiong, Q., Baychev, T. G., & Jivkov, A. P. (2016). Review of pore network modelling of porous media:
955 Experimental characterisations, network constructions and applications to reactive transport.
956 *Journal of Contaminant Hydrology, 192*, 101-117.
957 doi:http://dx.doi.org/10.1016/j.jconhyd.2016.07.002
958
959 Zeng, Z., & Grigg, R. (2006). A Criterion for Non-Darcy Flow in Porous Media. *Transport in Porous Media,*
960 *63*(1), 57-69. doi:10.1007/s11242-005-2720-3

Zhang, J., & Xing, H. (2012). Numerical modeling of non-Darcy flow in near-well region of a geothermal reservoir. *Geothermics, 42*, 78-86. doi:https://doi.org/10.1016/j.geothermics.2011.11.002

Zimmerman, R. W., Al-Yaarubi, A., Pain, C. C., & Grattoni, C. A. (2004). Non-linear regimes of fluid flow in rock fractures. *International Journal of Rock Mechanics and Mining Sciences, 41*, 163-169. doi:https://doi.org/10.1016/j.ijrmms.2004.03.036